



Defense Threat Reduction Agency
8725 John J. Kingman Road, MS
6201 Fort Belvoir, VA 22060-6201



DTRA-TR-16-67

TECHNICAL REPORT

2D and 3D Multiscale/Multicomponent Modeling of Impact Response of Heterogeneous Energetic Composites

Distribution Statement A. Approved for public release; distribution is unlimited.

June 2016

HDTRA1-10-1-0039

Min Zhou et al.

Prepared by:
Georgia Institute of
Technology
801 Ferst Dr, MRDC 4108
Atlanta, GA 30309

DESTRUCTION NOTICE:

Destroy this report when it is no longer needed.
Do not return to sender.

PLEASE NOTIFY THE DEFENSE THREAT REDUCTION
AGENCY, ATTN: DTRIAC/ J9STT, 8725 JOHN J. KINGMAN ROAD,
MS-6201, FT BELVOIR, VA 22060-6201, IF YOUR ADDRESS
IS INCORRECT, IF YOU WISH IT DELETED FROM THE
DISTRIBUTION LIST, OR IF THE ADDRESSEE IS NO
LONGER EMPLOYED BY YOUR ORGANIZATION.

REPORT DOCUMENTATION PAGE				Form Approved OMB No. 0704-0188	
<p>The public reporting burden for this collection of information is estimated to average 1 hour per response, including the time for reviewing instructions, searching existing data sources, gathering and maintaining the data needed, and completing and reviewing the collection of information. Send comments regarding this burden estimate or any other aspect of this collection of information, including suggestions for reducing the burden, to the Department of Defense, Executive Service Directorate (0704-0188). Respondents should be aware that notwithstanding any other provision of law, no person shall be subject to any penalty for failing to comply with a collection of information if it does not display a currently valid OMB control number.</p> <p>PLEASE DO NOT RETURN YOUR FORM TO THE ABOVE ORGANIZATION.</p>					
1. REPORT DATE (DD-MM-YYYY) 00-06-2016		2. REPORT TYPE Final Report		3. DATES COVERED (From - To) April 12, 2010 - Oct 15, 2015	
4. TITLE AND SUBTITLE 2D and 3D Multiscale/Multicomponent Modeling of Impact Response of Heterogeneous Energetic Composites				5a. CONTRACT NUMBER	
				5b. GRANT NUMBER HDTRA1-10-1-0039	
				5c. PROGRAM ELEMENT NUMBER	
6. AUTHOR(S) Zhou, Min; Kim, Seokpum; Wei, Yaochi				5d. PROJECT NUMBER HDTRA1-10-1-0039	
				5e. TASK NUMBER	
				5f. WORK UNIT NUMBER	
7. PERFORMING ORGANIZATION NAME(S) AND ADDRESS(ES) Woodruff School of Mechanical Engineering, Georgia Institute of Technology 801 Ferst Dr., MRDC 4108, Atlanta, GA 30309 USA				8. PERFORMING ORGANIZATION REPORT NUMBER	
9. SPONSORING/MONITORING AGENCY NAME(S) AND ADDRESS(ES) Defense Threat Reduction Agency 8725 John J. Kingman Road Fort Belvoir, VA 22060-6201 USA				10. SPONSOR/MONITOR'S ACRONYM(S) DTRA	
				11. SPONSOR/MONITOR'S REPORT NUMBER(S) DTRA-TR-16-67	
12. DISTRIBUTION/AVAILABILITY STATEMENT Distribution Statement A. Approved for public release; distribution is unlimited.					
13. SUPPLEMENTARY NOTES					
14. ABSTRACT This report summarizes the outcome of research performed under project entitled 2D and 3D Multiscale/Multicomponent Modeling of Impact Response of Heterogeneous Energetic Composites (HDTRA1-10-1-0039). The primary achievements are (1) the development of a computational platform for simulating the impact ignition behavior of a class of heterogeneous energetic materials (HEM) that are known as polymer-bonded explosives and granular explosives, (2) quantification of the ignition behavior of such materials impact loading, (3) computational capabilities for generating statistically consistent microstructure sets of HEM, and (4) establishment of relations between the ignition probabilities of HEM as function of loading and microstructure.					
15. SUBJECT TERMS kinetics; dynamic impact loading; polymer bonded explosives; shear banding					
16. SECURITY CLASSIFICATION OF:			17. LIMITATION OF ABSTRACT SAR	18. NUMBER OF PAGES	19a. NAME OF RESPONSIBLE PERSON Allen Dalton
a. REPORT U	b. ABSTRACT U	c. THIS PAGE U			19b. TELEPHONE NUMBER (Include area code) 703-767-3054

UNIT CONVERSION TABLE

U.S. customary units to and from international units of measurement^{*}

U.S. Customary Units	<div style="display: flex; align-items: center; justify-content: center;"> <div style="margin-right: 10px;"> </div> Multiply by </div> <div style="display: flex; align-items: center; justify-content: center;"> <div style="margin-right: 10px;"> </div> Divide by[†] </div>	International Units
Length/Area/Volume		
inch (in)	2.54 $\times 10^{-2}$	meter (m)
foot (ft)	3.048 $\times 10^{-1}$	meter (m)
yard (yd)	9.144 $\times 10^{-1}$	meter (m)
mile (mi, international)	1.609 344 $\times 10^3$	meter (m)
mile (nmi, nautical, U.S.)	1.852 $\times 10^3$	meter (m)
barn (b)	1 $\times 10^{-28}$	square meter (m ²)
gallon (gal, U.S. liquid)	3.785 412 $\times 10^{-3}$	cubic meter (m ³)
cubic foot (ft ³)	2.831 685 $\times 10^{-2}$	cubic meter (m ³)
Mass/Density		
pound (lb)	4.535 924 $\times 10^{-1}$	kilogram (kg)
unified atomic mass unit (amu)	1.660 539 $\times 10^{-27}$	kilogram (kg)
pound-mass per cubic foot (lb ft ⁻³)	1.601 846 $\times 10^1$	kilogram per cubic meter (kg m ⁻³)
pound-force (lbf avoirdupois)	4.448 222	newton (N)
Energy/Work/Power		
electron volt (eV)	1.602 177 $\times 10^{-19}$	joule (J)
erg	1 $\times 10^{-7}$	joule (J)
kiloton (kt) (TNT equivalent)	4.184 $\times 10^{12}$	joule (J)
British thermal unit (Btu) (thermochemical)	1.054 350 $\times 10^3$	joule (J)
foot-pound-force (ft lbf)	1.355 818	joule (J)
calorie (cal) (thermochemical)	4.184	joule (J)
Pressure		
atmosphere (atm)	1.013 250 $\times 10^5$	pascal (Pa)
pound force per square inch (psi)	6.984 757 $\times 10^3$	pascal (Pa)
Temperature		
degree Fahrenheit (°F)	[T(°F) – 32]/1.8	degree Celsius (°C)
degree Fahrenheit (°F)	[T(°F) + 459.67]/1.8	kelvin (K)
Radiation		
curie (Ci) [activity of radionuclides]	3.7 $\times 10^{10}$	per second (s ⁻¹) [becquerel (Bq)]
roentgen (R) [air exposure]	2.579 760 $\times 10^{-4}$	coulomb per kilogram (C kg ⁻¹)
rad [absorbed dose]	1 $\times 10^{-2}$	joule per kilogram (J kg ⁻¹) [gray (Gy)]
rem [equivalent and effective dose]	1 $\times 10^{-2}$	joule per kilogram (J kg ⁻¹) [sievert (Sv)]

^{*} Specific details regarding the implementation of SI units may be viewed at <http://www.bipm.org/en/si/>.

[†] Multiply the U.S. customary unit by the factor to get the international unit. Divide the international unit by the factor to get the U.S. customary unit.

Final Report

for

DTRA Project Number HDTRA1-10-1-0039

**2D and 3D MULTISCALE/MULTICOMPONENT MODELING OF
IMPACT RESPONSE OF HETEROGENEOUS ENERGETIC
COMPOSITES**

submitted to

Dr. Douglas Allen Dalton
Defense Threat Reduction Agency
J9-BAS, Cube 3650D
8725 Kingman Road, Fort Belvoir, VA 22060
Tel: (703) 767-3054, Fax: (703) 767-3335

by

Min Zhou
Principal investigator
The Woodruff School of Mechanical Engineering &
The School of Materials Science and Engineering
Georgia Institute of Technology
Atlanta, GA 30332-0405
Tel: 404-894-3294, Fax: 404-894-0186
min.zhou@gatech.edu

October 15, 2015

Table of Contents

Objectives, Scope, Milestones, and Tasks/Scientific Goals	2
Scientific Accomplishments	7
Development of Cohesive Finite Element Method (CFEM) Capability	7
3D Modelling of Impact Response of HMX Granule Aggregates	10
Hotspot Quantification and Ignition Criterion	15
Prediction of Probabilistic Ignition Behavior of PBXs.....	20
Quantification of the Ignition Probability as a Function of Random Variations in Microstructural Morphology and Inter-constituent Bonding.....	28
Quantification of the Effect of Viscoplasticity on Ignition Sensitivity	34
Ignition Desensitization of PBX via Aluminization	40
Ignition Behavior of an Aluminum-Bonded Explosives (ABX)	44
References.....	47
Training and Professional Development.....	49
Dissemination of the Results	50

Grant/Award #:	HDTRA1-10-1-0039
PI Name:	Min Zhou
Organization/Institution:	Georgia Institute of Technology
Project Title:	2D and 3D Multiscale/Multicomponent Modeling of Impact Response of Heterogeneous Energetic Composites

What are the major goals of the project?

List the major goals of the project as stated in the approved application or as approved by the agency. If the application lists milestones/target dates for important activities or phases of the project, identify these dates and show actual completion dates or the percentage of completion. Generally, the goals will not change from one reporting period to the next. However, if the awarding agency approved changes to the goals during the reporting period, list the revised goals and objectives. Also explain any significant changes in approach or methods from the agency approved application or plan.

Objectives

The objective of this project as modified and approved by DTRA is to develop a new scientific framework and technical capability for the computational analyses and design of the thermal-mechanical behavior of energetic composite materials under dynamic impact loading. The model material system polymer bonded explosives (PBX). The capability to be developed goes beyond what is available at the present. Due to the reduced level of funding available relative to the level in the original proposal, we have made certain changes in the scope of the work. The characteristics of the framework and capability include (1) focus on our state-of-the-art 2D CFEM computational framework, (2) account of fully dynamic finite deformation kinetics and kinematics, (3) tracking of microstructural level fracture, failure, shear banding, contact and frictional heating, (4) account for the coupling between mechanical deformation and thermal generation and conduction, (5) account for the initiation of energetic reactions in dynamically deforming heterogeneous materials, (6) characterization of the stochastic variations in ignition behavior, and (7) three-dimensional (3D) modeling will primarily focus on the effect of anisotropic crystalline plastic response (slip) on the dissipation mechanisms in HMX granule aggregates.

Scope

The tasks of this project focus on (1) developing a model to analyze hotspot dynamics—rate of temperature increase, spatial distribution of hotspots generated—as functions of variations in microstructure and constituent properties; (1) developing an approach for quantifying the stochastic variations in the response of energetic materials as functions of variations in microstructure and constituent properties (2) establishing relationships between the ignition response of heterogeneous energetic materials and their microstructures (formulation); (3) verifying and validating the relations through open-literature (3) continuing to transfer software technology and material design relations developed to the AFRL/RWME and other national labs.

Milestones and Schedule

Year #1: (Completed)

- Formulation of 3D equations of deformations, heat production & transfer, thermal – mechanical coupling, and constitutive and interfacial behaviors;
- Implementation of models in CFEM codes (CODEX suite of codes).

Year #2: (Completed)

- 3D CFEM code developed
- Preliminary CFEM calculations carried out;
- Novel hotspot quantification method developed;

Year #3: (Completed)

- Simulations for constitutive and interfacial characterization;
- CFEM continuum modeling;
- Transfer of CFEM code to AFRL/RWME as appropriate;
- Ignition criterion developed.

Year #4: (Completed)

- Effects of microstructure, constituents, composition and loading characterized through CFEM simulations – focus on 2D modeling approach, ignition threshold and probabilistic nature of ignition, and effect of microstructure variation on uncertainty in ignition behavior;

Year #5: (Completed)

- A statistical hot-spot formation and evolution model developed;
- Quantification of the ignition probability as a function of microstructural attributes (e.g., volume fraction of constituents or specific surface area), variations in microstructure, inter-constituent bonding, and loading condition.
- Formulation of microstructure-ignition relations developed as a preliminary capability for PBX materials design;

Performance Schedule

Detailed Task	Description	Year 1	Year 2	Year 3	Year 4	Year 5
(1)	Development of 2D&3D CFEM model and software capability	Completed				
(2)	Approach for determining constituent and interfacial properties		Completed			
(3)	Development of a framework for analyzing energetic reactions		Completed			
(4)	Characterization of the effects of microstructure and constituents			Completed		
(5)	Development of microstructure-performance relations				Completed	

Tasks/Scientific Goals

Task 1 – Development of the Cohesive Finite Element Method (CFEM) framework

A new scientific framework and technical capability is developed for the computational analyses of the thermal-mechanical behavior of energetic composite materials under dynamic impact loading. The capability to be developed goes beyond what is available at the present. Characteristics of the framework and capability include (1) account for the microstructural morphology of energetic composite materials such as polymer-bonded explosives (PBX), (2) account of fully dynamic finite deformation kinetics and kinematics, (3) tracking of microstructural level fracture, failure, shear banding, contact and frictional heating, (4) account for the coupling between mechanical deformation and thermal generation and conduction, and (5) account for the energetic reactions in dynamically deforming heterogeneous materials.

Task 2 – Three-Dimensional Modelling of Impact Response of Heterogeneous Explosives

This novel computational simulation capability should be able to consider (1) polycrystalline material structures, (2) random and textured grain orientation distributions, (3) anisotropic elastic and crystal plastic slip responses of molecular crystals such as HMX and RDX, and (4) full coupling of mechanical deformation and heat generation/conduction. An algorithm for the generation of polycrystal microstructures with prescribed grain sizes, shapes, and size distributions is established. The effects of polycrystalline structure, crystalline slip and statistical variation in microstructure level behavior on hotspot formation is quantified.

Task 3 – Development of a Hotspot Quantification Model and the Ignition Threshold

A systematic method is developed for the statistical quantification of hotspot fields resulting from non-shock impact loading of GXs and PBXs. This new method quantifies the distributions of the size and shape of hotspots and distances between hotspot as function of microstructures and loading using Radial Distribution Function (RDF). The second development is a new criterion for establishing the ignition conditions of heterogeneous energetic materials under general conditions. This criterion, similar to a “yield” or failure criterion in mechanics of materials, links the hotspot size-temperature states in a loading event to the threshold size-temperature conditions of hotspots, which are regarded as materials properties. The relation between the grain size and the material sensitivity (i.e., ignition) is obtained.

Task 4 – *The effect of variations in microstructural uncertainties on ignition behavior using a probabilistic approach*

An approach for computationally predicting and quantifying the stochasticity of the ignition process in polymer-bonded explosives under impact loading is developed. The method involves subjecting sets of statistically similar microstructure samples to identical overall loading and characterizing the statistical distribution of the ignition response of the samples. The analyses focus on the influence of random microstructure geometry variations on the critical time to ignition and the critical impact velocity below which no ignition occurs. The relation between the microstructural attributes (e.g., grain size distribution, specific surface area, and HMX grain volume fraction) and the ignition probability is obtained.

Task 5 – *Quantification of the Ignition Probability as a Function of Random Variations in Microstructural Morphology and Inter-constituent Bonding*

Accounting for the combined effect of multiple sources of stochasticity in material attributes, we develop an approach that computationally predicts the probability of ignition of polymer-bonded explosives (PBXs) under impact loading. The analysis focuses on the effects of two sources of stochastic variations at the microstructural level on hotspot development in a PBX. The random variations considered are associated with the morphologies of constituent phases and the bonding strength of the grain-binder interfaces. The probability of ignition arising from one source of stochastic variation is quantified and analyzed separately from another source. The two probability functions are then combined using relations between the time to criticality and microstructure attributes.

Task 6 – *Effects of constituent properties and composition of PBX on ignition behavior*

Three separate analyses are performed to study the effect of constituent properties and composition of PBX on ignition behavior. First, the role of viscoplasticity of HMX in PBX is analyzed by comparison of impact responses between elastic HMX based PBX and viscoplastic HMX based PBX. Second, ignition desensitization of PBX via aluminization is analyzed. Third, a hypothetical energetic composite is proposed. The

new composite is aluminum bonded explosive (ABX) which composes of HMX grains suspended in an aluminum matrix.

What was accomplished under these goals?

For this reporting period describe: 1) major activities; 2) specific objectives; 3) significant results, including major findings, developments, or conclusions (both positive and negative); and 4) key outcomes or other achievements. Include a discussion of stated goals not met. As the project progresses, the emphasis in reporting in this section should shift from reporting activities to reporting accomplishments.

Development of Cohesive Finite Element Method (CFEM) Capability

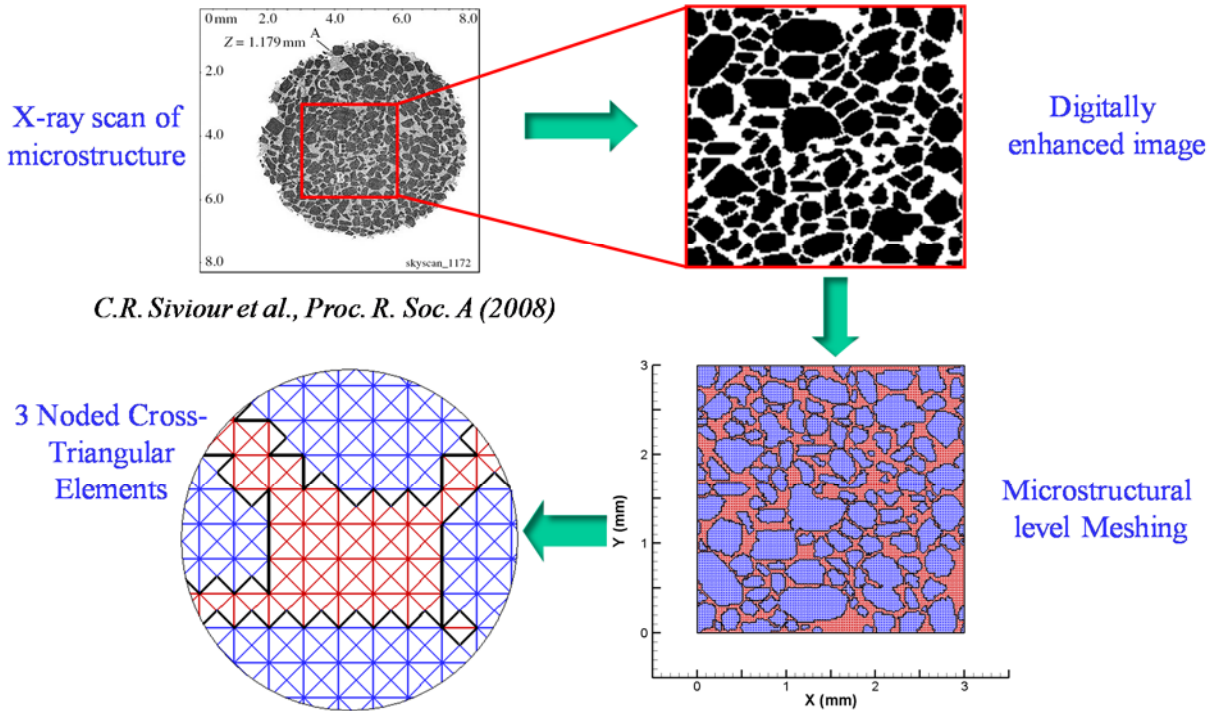


Fig. 1 The CFEM approach for analysis of thermomechanical response of PBXs.

A cohesive finite element method (CFEM) based framework is developed and used, in which, cohesive elements are embedded throughout the microstructure, along all elements boundaries. This approach allows arbitrary fracture paths and patterns inside each phase and along the interfaces between the phases to be resolved. This form of CFEM obviates the need for criteria for fracture initiation and propagation but requires the model to satisfy limitations on mesh density and cohesive stiffness [1]. Contact and friction between failed crack surfaces are accounted for, allowing heating due to interfacial sliding to be analyzed along with heating due to bulk constitutive inelasticity. The framework entails a fully coupled thermal-mechanical formulation. Therefore, the interactions between the mechanical process of dynamic deformation and failure and the thermal process of heat generation and conduction are resolved. A range of actual and idealized microstructures with varying attributes are considered in order to establish relationships between microstructural features such as grain size, distribution and contiguity and the stress-strain response, failure and heating. The objective is to formulate microstructure – properties relations in a manner that lends them to the design and development of PBXs with tailored property attributes. Figure 1 illustrates the CFEM approach for the analysis of thermomechanical response of PBXs.

A systematic analysis is carried out using the actual PBX micrograph. Figure 2 shows the distributions of the equivalent stress. The HMX grains, which are stiffer than the binder, sustain higher stresses. The grains are not uniformly stressed – higher stresses are seen for grains which are part of one of the ‘force chains’, as outlined in Fig. 2(a). These force chains can be regarded as assemblies of grains positioned such that they support higher levels of compressive and shear stresses. The overall level of stress in the microstructure increases with the progression of deformation until interfacial debonding and transgranular fracture initiate. Figure 2(b) shows the evolution of temperature. Initially, viscous dissipation in the soft binder is primarily responsible for the temperature increase. The hard grains cause more intense deformation in the binder, leading to localized regions of high temperatures. As time progresses, these regions coalesce to form shear bands which tend to extend diagonally through the microstructure, approximately following the direction of maximum shear stress.

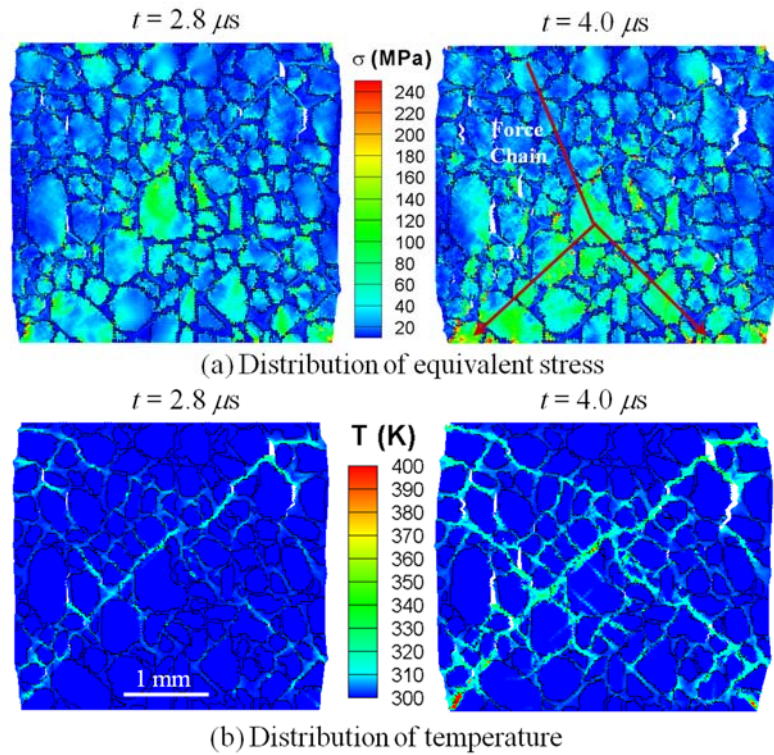


Fig. 2 Evolution of (a) equivalent stress and (b) temperature in the PBX microstructure

The primary findings of the analysis using the CFEM framework are:

- (1) while viscoelastic dissipation plays the most important role in heating in early stages of impact events, frictional heating eventually take over and dominant the heating process;
- (2) heating overall becomes more severe as packing density increases and the most severe heating in binder occurs for a packing density of around 0.69 at $T = 300 \text{ K}$;
- (3) bimodal distribution of grain size increases heating and hot-spot formation primarily because of enhanced interactions between the energetic granules;
- (4) more severe heating occurs when temperature $T < T_g$ (glass transition temperature) because the binder is harder and more brittle at lower temperatures;

- (5) at $T = 300\text{ K}$ ($> T_g$), lower impact velocities (lower loading rates) correspond to more heating in binder and grains - since the binder is less stiff due to viscoelasticity, it deforms more and allows grain-grain interactions;
- (6) lateral confinement (hydrostatic stress) decreases failure and dissipation along cracks initially but eventually leads to more fractional heating along crack faces at later times;
- (7) for a confined specimen, a decrease in interfacial strength causes higher frictional dissipation due to grain-matrix debonding; while in an unconfined specimen, the interfacial bonding strength has no appreciable effect; and
- (8) heating mechanism and mechanism transition may affect the distribution more than packing density, loading rate, or stress state.

3D Modelling of Impact Response of HMX Granule Aggregates

The polycrystalline model here can be regarded as an idealization of PBXs in which the thickness of the binder between adjacent grains is much smaller than the size of the grains so that it is taken to be zero. This approach simplifies the material condition and allows us to delineate the effect of intrinsic material anisotropy on the behavior of the overall material. The ensemble of crystals is generated using the relaxed dual complex (RDC) method proposed by Rimoli and Ortiz [2]. The RDC method takes as input an initial triangulation of the domain. The triangulation is then refined appropriately to provide suitably sized grains. The grain ensemble is geometrically arranged into a regular packing of two distinct grain morphologies and sizes, as seen in Fig. 3. The resulting microstructure is a polycrystalline HMX with each grain having a random crystallographic orientation.

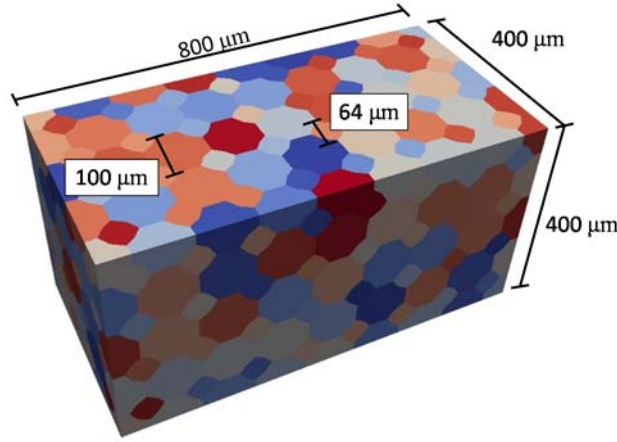


Fig. 3 Configuration for 3D microstructure model

Two models with different numbers of available slip systems are used, reflecting differing characterizations of the slip systems of the HMX molecular crystal. Figure 4 illustrates all seven slip systems used by Barton et al. [3], and the slip systems labeled in green also correspond to the two systems used by Zamiri [4].

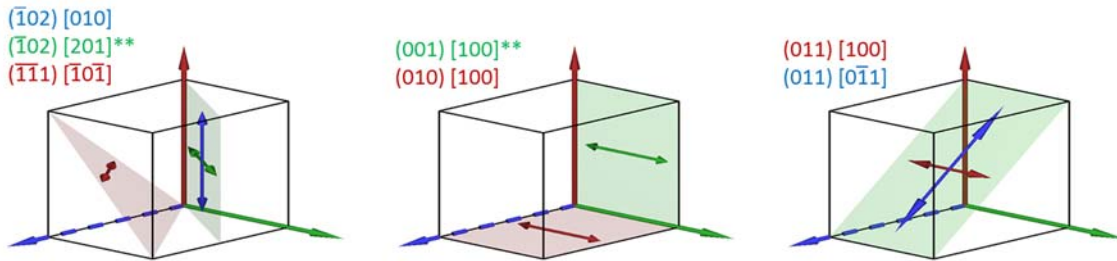


Fig. 1 The seven potential slip systems of HMX crystal in the $P21/c$ space. **The Zamiri case involves only the two slip systems labeled in green. The Barton case involves all seven potential slip systems shown here.

The framework allows us to fully quantify of the effects of (1) the structure of crystalline slip systems in HMX and (2) the microstructural level crystalline anisotropy on the conditions in energetic materials under prescribed loading and boundary conditions. The primary findings of the analysis using 3D model are:

- (1) The effect of the number of available slip systems on the stress fields in polycrystalline HMX is shown in Fig. 5. The average stress is nearly linearly related to the impact velocity for both material descriptions, a feature that is seen in high velocity impact experiments. The figure also shows that the mean stress is consistently higher in the Zamiri (2 slip systems) case than in the Barton (7 slip systems) case. This effect increases with impact velocity from 4.5% at 50 m/s to 16.2% at 400 m/s. This is due to the fact that the Zamiri case has limited avenues for dissipating energy via plastic slip, resulting in elevated stresses due to nearly elastic behavior in many loading orientations. The Barton case, however, is capable of accommodating plastic slip in any orientation, resulting in lower stresses.

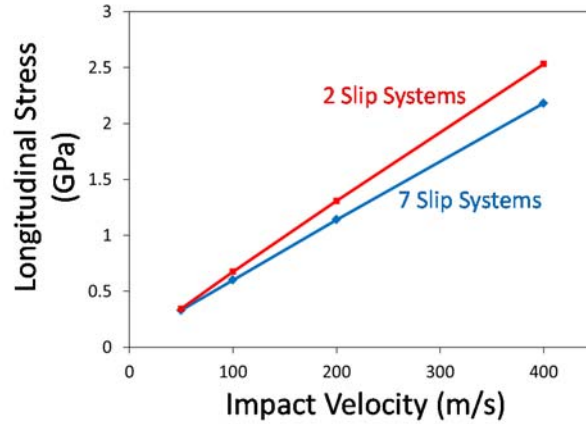


Fig. 5 Plateau stress as a function of impact velocity. The 2 slip system case (left) is shown to have a lower plateau stress than the 7 slip system case (right) for all impact velocities, and both increase with velocity in a linear manner.

- (2) The distribution of stress states in the domain is quantified. Figure 6 shows the normalized standard deviation of stress as a function of impact velocity for both material cases. For all velocities, the Zamiri case displays greater variation in stress state than the Barton case. This allows a relationship between the heterogeneity of the material domain and the variability in the stress field (in the form of normalized standard deviation) to be drawn. The more heterogeneity that exists in a material microstructure, the greater the expected variation in observed stress states should be. The lower bound of this phenomenon is simply the case of a homogeneous crystal loaded uniaxially; in this case, the theoretical stress state will not vary on any given material cross-section perpendicular to the loading axis. When grains in the Zamiri case are simulated as a heterogeneous ensemble, stress concentrations due to significant anisotropy in the material model are caused by the orientation of the individual crystals. In the Barton case, however, the difference between the most and least preferential directions in each grain is relatively low, creating a system

that is anisotropic, but has less directional variation than the Zamiri case. Another noticeable trend in Fig. 6 is that the Zamiri case increases in variability with impact velocity while the response of the Barton case becomes more homogeneous. The decrease in variability with increased impact velocity seen in the Barton case is in general agreement with the results by Baer [5] of a mock PBX under shock loading. Figure 7 shows the normalized maximum stresses for both cases as a function of impact velocity. The Zamiri cases have maximum stresses between 1.6 and 1.9 times the bulk averaged stress and the maximum stresses for the Barton cases are between 1.3 and 1.6 times higher than the average stress. The Zamiri case has greater variability in stress states for all impact velocities, as well as, a greater difference between the average stress and the extreme stress state. This indicates that the greater the anisotropy of the underlying crystal structure, the less capable that a homogenized response is of reliably modeling the local material response. This quantitative analysis of the stress field distribution allows us to clearly see the influence that the number of slip systems has on the variability of the longitudinal stress behind the stress wave.

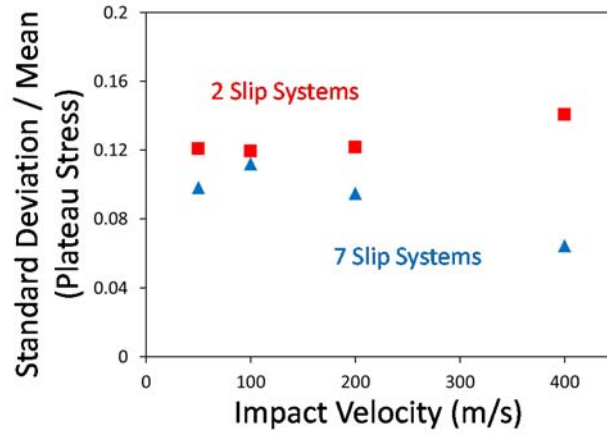


Fig. 6 Data points measure the uniformity of the longitudinal stress field in the plateau region behind the stress wave. The data show that as heterogeneity in the material increases due to material anisotropy, a wider range of stress states is seen in the material.

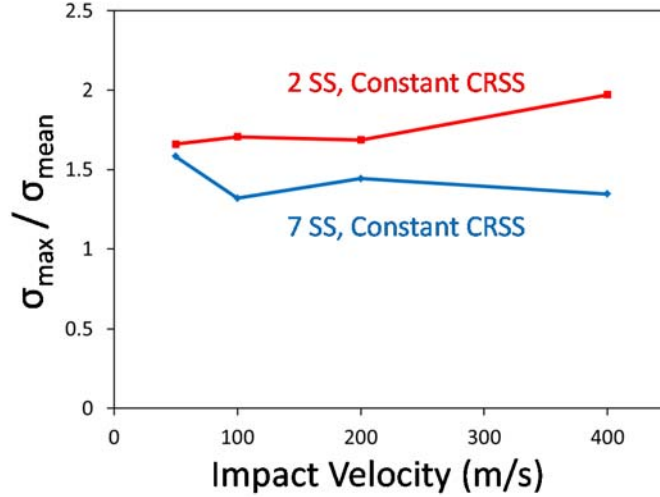


Fig. 7 Maximum longitudinal stress normalized by the averaged stress in the plateau region behind the stress front is here plotted as a function of impact velocity for 2 and 7 available slip systems. This plot clearly demonstrates the spread of the extreme values observed in the material.

- (3) The effect on the variability of the temperature field due to crystalline anisotropy has also been quantified. Figure 8 summarizes the temperatures for both slip system cases with constant and variable CRSS. Figure 8(a) shows that the average temperature increases monotonically for both cases as imposed velocity increases and the rate of temperature increase is slightly higher at higher imposed velocities. The Barton case exhibits higher average temperatures at all imposed boundary speeds than Zamiri case. The higher rate of average heating in the Barton case is due to the enhanced availability of slip systems relative to the Zamiri case. Figure 8(b) indicates that the peak temperatures are not strongly dependent on the number of slip systems. The similarity between Barton case and Zamiri case is due to both material descriptions sharing the (001)[100] system, which has the highest CRSS. Therefore, the peak temperature rise in both material cases is associated with the strongest slip system which yields the highest temperature change for the same amount of slip.

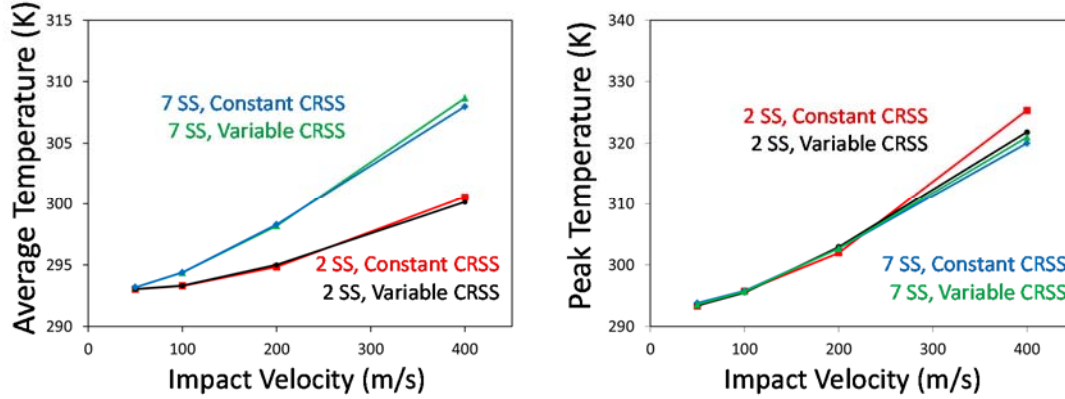


Fig. 8 (a) Average temperature in the plateau region and (b) Peak specimen temperature function of impact velocity and CRSS.

- (4) The effect of varying the critical resolved shear stress (CRSS) for each available slip system is analyzed for both material descriptions. For this set of simulations, we explicitly vary the CRSS of each slip system on an element by element basis such that their distribution is described by a random normal distribution having a mean equal to the reported value in the literature and a standard deviation equal to 15 percent of the mean value. The results from these simulations are then compared to those with constant CRSS. The simulations with variation of the CRSS show negligible effect on the average stress, the range or distribution of stresses, or the transversely averaged temperature. The average stress obtained using variable CRSS differs by less than 1.5% for all impact velocities from that obtained using a constant CRSS in each element. Likewise, the normalized standard deviation and normalized maximum stress both fall within 8.0 % of the constant CRSS as well. Average temperatures behave similarly, exhibiting no more than 1.1 degrees difference in temperature rise. Varying the CRSS has very little effect on the behavior of the material as a whole because the response of the material in this loading regime is dominated by the crystalline orientation. The strongest slip system is approximately 4.5 times stronger than the weakest system. Therefore varying a given system strength by as much as 50% would still have less of an influence on the mechanical response of a crystal than rotating it to a more/less favorable orientation. This result implies that the effect of variation in material strength is made insignificant by the effect of orientation dependent material behaviors such as anisotropic elasticity and crystal plasticity.

Hotspot Quantification and Ignition Criterion

Our effort to characterize the effects of microstructure and constituents on response for the purpose of materials design has focused on a systematic study of both granular HMX (GXs) and polymer-bonded explosives (PBXs) which have two-phase microstructures consisting of HMX grains and an Estane binder. Actual microstructures are used to model the PBX, as shown in Fig. 9(a). Additionally, a set of five idealized microstructures are used to model granular HMX. These samples are generated using monomodal and bimodal size distributions of spherical grains [representative micrographs are shown in Figs. 9(b-f)].

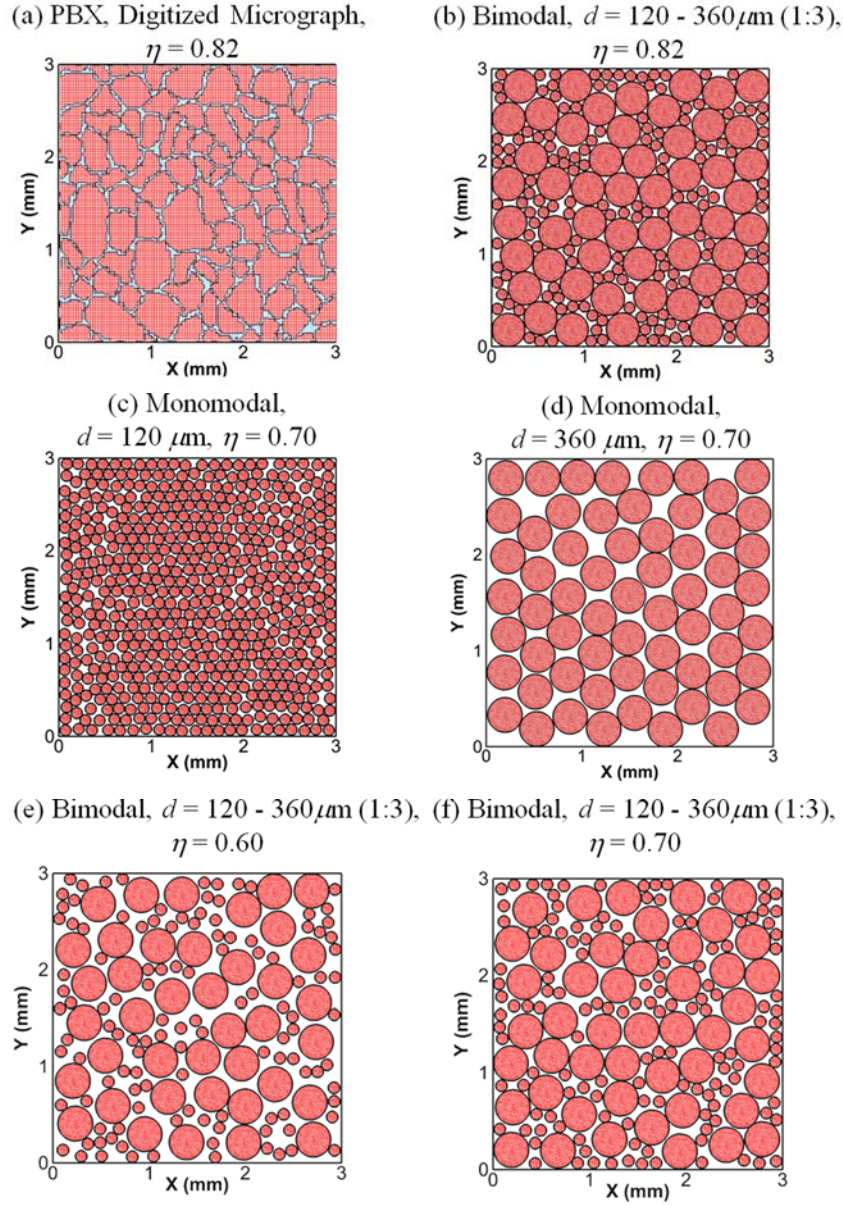


Fig. 9 Examples of microstructures analyzed -- digitized image of a PBX and idealized microstructures for granular HMX with different grain size distributions, (a) Digitized image of

a PBX, *(b)* bimodal GX, $d = 120 - 360 \mu\text{m}$, $\eta = 0.82$, *(c)* monomodal GX, $d = 120 \mu\text{m}$, $\eta = 0.70$, *(d)* monomodal GX, $d = 120 \mu\text{m}$, *(e)* bimodal GX, $d = 120 - 360 \mu\text{m}$, $\eta = 0.60$ and *(f)* bimodal GX, $d = 120 - 360 \mu\text{m}$, $\eta = 0.70$.

Hotspot Quantification using Radial Distribution Function (RDF):

We have developed a novel scheme for the characterization of hotspot fields resulting from shock and non-shock impact loading of granular explosives (GXs) and polymer-bonded explosives (PBXs), although current analyses solely focus on non-shock loading. This new method uses the radial distribution function (RDF) and yields quantifications of the distributions of the size and shape of hotspots and distances between hotspot as function of microstructures and loading [see Figs. 10(a-f)]. When different temperature threshold (ΔT_{thres}) values are used, hotspots with specific characteristics can be identified.

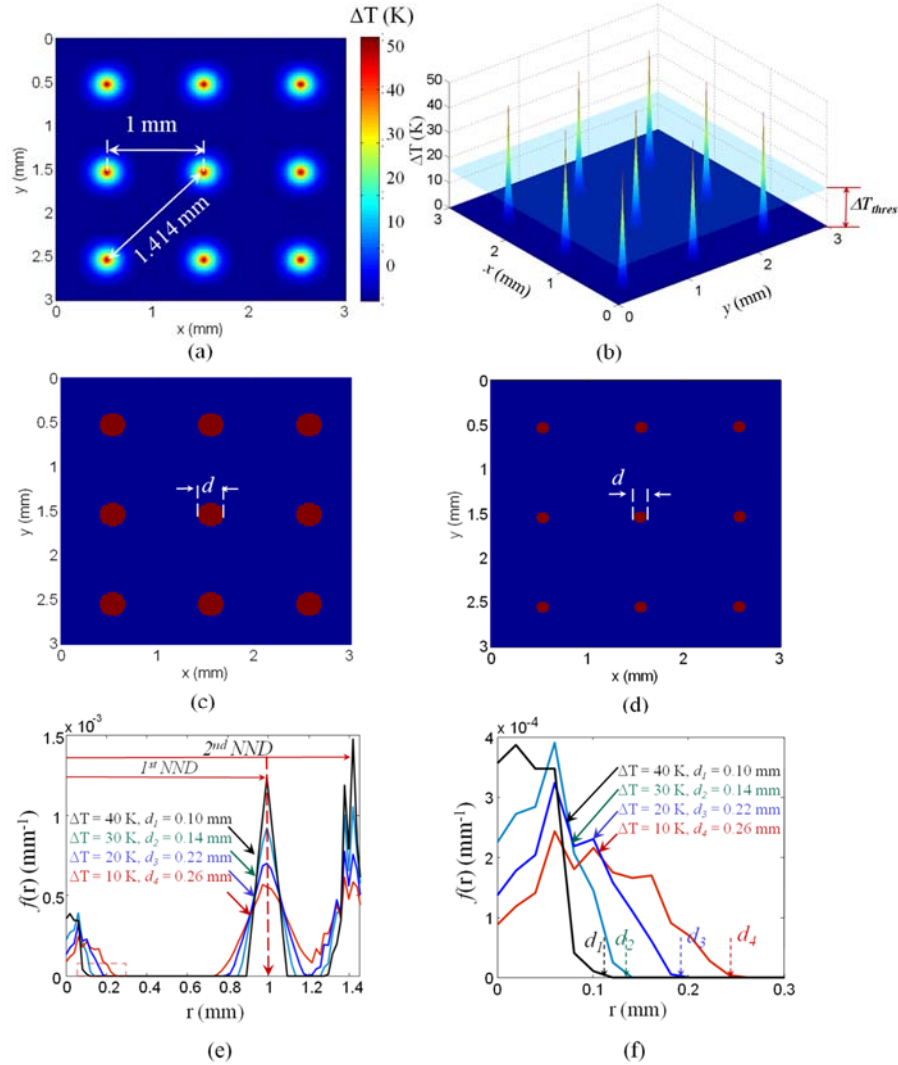


Fig. 10 Illustration and quantification of an idealized hotspot field, (a) hotspots arranged in a regular square array, (b) 3D temperature profile of the idealized hotspots field, and a schematic

sectioning of the hotspot field by a plane at a given cutoff temperature, $\Delta T_{thres.}$, (c) hotspots on section with $\Delta T_{thres} = 15$ K, (d) hotspots on section with $\Delta T_{thres} = 30$ K, (e) radial distribution function (RDF) of the idealized hotspot distribution at different cutoff temperatures, and (f) a close-up view of the region where the RDFs go to zero which shows the diameter of the hotspots at the corresponding cutoff temperatures.

The hotspot distributions are systematically analyzed using the threshold scheme shown in Fig. 10. Major findings from this analysis are:

- (1) Effect of Initial Porosity: For GXs, initial porosity plays the most important role in heating in terms of heating rate but not hot-spot size and spacing.
- (2) Effect of Grain Size: For GXs with different grain sizes (monomodal, bimodal), the maximum size of hotspot (d_{max}) varies only slight among the cases [see Fig. 11(a)], suggesting that ignition sensitivity is not significantly affected by grain size. However, the bimodal distribution shows highest average spacing between hotspots (l_{avg}) than monomodal size distributions.
- (3) Effect of Impact Velocity: The maximum size of hotspot (d_{max}) does not change significantly over $v = 50 - 150$ ms⁻¹ [see Fig. 11(b)]. However, as the impact velocity increases beyond $v = 150$ ms⁻¹, d_{max} starts to decrease. This suggests that the hotspots tend to become more localized at higher loading rates. As v increases, the average hotspot spacing l_{avg} decreases approximately linearly.

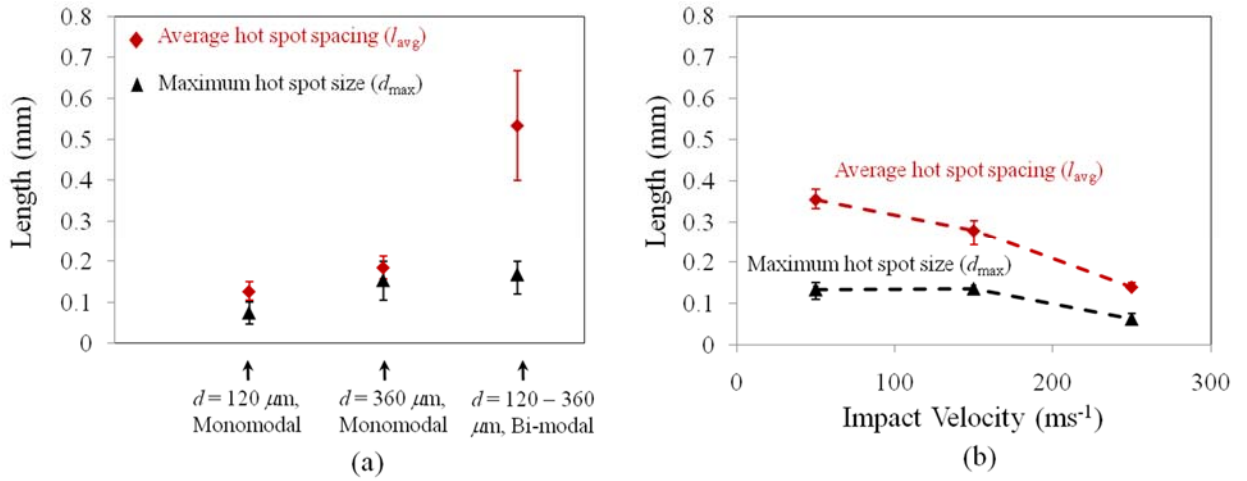


Fig. 11 (a) Effect of grain size on the maximum hotspot size and average hotspot spacing [GX in Figs. 9(c-d, f)], $\eta = 0.70$, $v = 100$ ms⁻¹, $\dot{\epsilon} = 33.3 \times 10^3$ s⁻¹, and (b) effect of impact velocity on the maximum hotspot size and average hotspot spacing ($\eta = 0.82$, bimodal GX, $v = 50 - 250$ ms⁻¹, $\dot{\epsilon} = 16.7 - 83.3 \times 10^3$ s⁻¹).

Hotspot Criticality Threshold:

We have developed a new criterion for establishing the ignition conditions of heterogeneous energetic materials under general conditions. This criterion, similar to a yield or failure criterion in mechanics of materials, links the hotspot size-temperature states in a loading event to the threshold size-temperature conditions of hotspots [6](Tarver 1996) which are regarded as materials properties. The criterion, along with the CFEM capability to quantify the thermal-mechanical behavior of GXs and PBXs, allows the critical impact velocity for ignition, time to ignition or delay time (t_c), and critical input energy at ignition to be determined as functions of material composition, microstructure and loading conditions. Results obtained using the threshold criterion include:

- (1) Wave reflections from confined boundaries (associated with small samples and larger impactors) multiply stress and temperature increases, making even low velocity impact dangerous if loading is maintained over sufficiently long durations. While for large samples (no wave reflections), GXs are more susceptible to ignition at all impact velocities than PBXs. For small, confined samples, GXs are more susceptible at high impact velocities, while PBXs are more susceptible at low impact velocities, when deformed to the same level of total strain. For the range of impact velocities considered ($v = 50 - 250 \text{ ms}^{-1}$), the PBXs are 2-4 times safer (in terms of critical impact velocity) than HMX at high impact velocities. The results are quantified in Fig. 12.

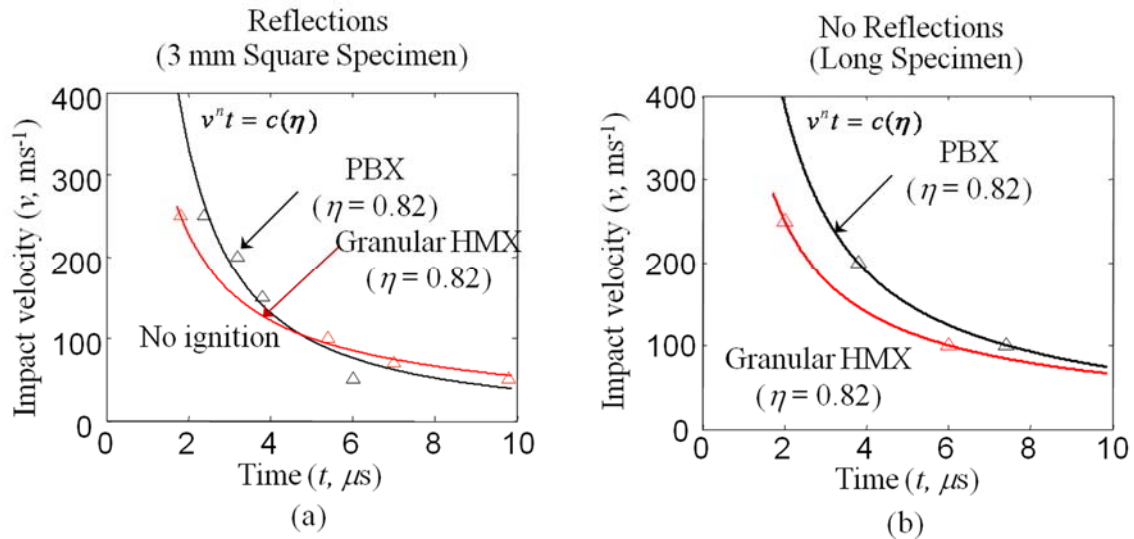


Fig. 12 Time to criticality for PBX and GX using (a) 3 mm square specimen and (b) long specimen ($\eta = 0.82$, $v = 50 - 250 \text{ ms}^{-1}$).

- (2) Overall, the higher the initial volume fraction η , the more sensitive the GX [see Figs. 13(a-b)]. The variation in response with η is small at high impact velocities, with a delay time of $t_c \sim 4 \mu\text{s}$ for all values of η considered. The similarity in response is due to the fact that at high impact velocities, grain fracture (and fragmentation) occurs almost immediately upon impact, leading to high temperature increases in the grains near the impact surface.

However, the sensitivity is significantly different at low impact velocities.

- (3) The times to criticality for microstructures with different grain sizes (monomodal, bimodal) overlap each other, indicating that the grain size distribution does not significantly affect ignition sensitivity [see Figs. 13(c-d)]. In all cases, the dominant heating mechanism is sliding friction at grain boundaries and at surfaces generated by grain fracture. At higher load intensities, there may be additional mechanisms (such as dislocations, phase transformation, and collapse of voids or defects) which may cause the response to be more sensitive to grain size or grain size distribution. Such factors shall be incorporated in the analysis in the future.

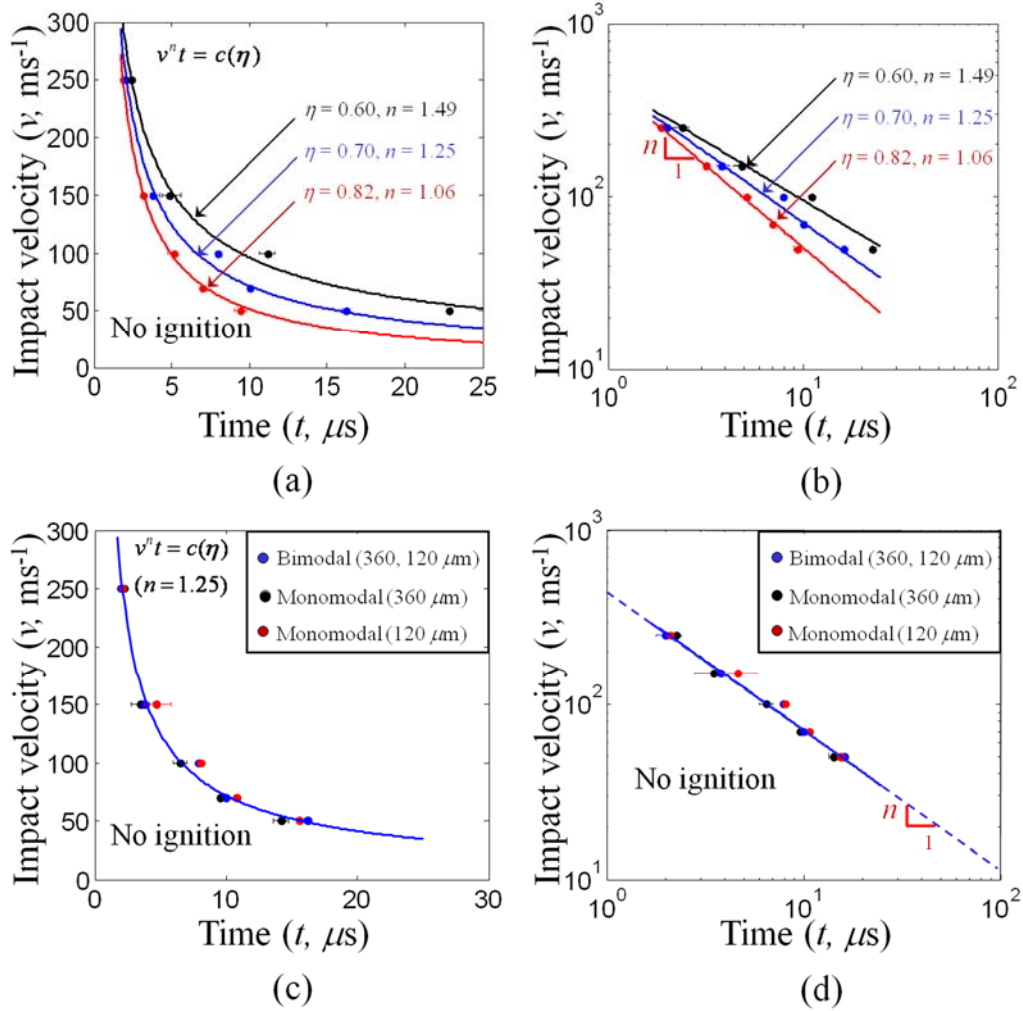


Fig. 13 Time to criticality for GX having a range of initial grain volume fractions $\eta = 0.60 - 0.82$, plotted using (a) linear scale (b) log-log scale ($\eta = 0.70 - 0.82$, $v = 50 - 250 \text{ ms}^{-1}$); time to criticality for GXs having different grain size distributions: monomodal, $d = 120 \mu\text{m}$, $d = 360 \mu\text{m}$, and bimodal, $d = 120 - 360 \mu\text{m}$, plotted using (c) linear scale (d) log-log scale ($\eta = 0.70$, $v = 50 - 250 \text{ ms}^{-1}$).

Prediction of Probabilistic Ignition Behavior of PBXs

A computational framework is developed to predict and quantify the stochasticity of the ignition process in polymer-bonded explosives (PBXs) which have two-phase microstructures consisting of HMX grains and an Estane binder. This framework involves the ignition criterion we have developed [7] for detecting critical hotspots which lead to thermal runaway, and measures time to criticality for the hotspots during impact loading. The sensitivity of a particular PBX composition is evaluated by performing numerical “experiments” on multiple instantiations of statistically similar microstructures. The variations at the microstructure level are related to the variations in the probability of ignition. Six different microstructural configurations are used to model PBXs. These microstructural configurations are generated using monomodal and bimodal size distributions of multi-faceted grains [representative micrographs are shown in Figs. 14(a-f)].

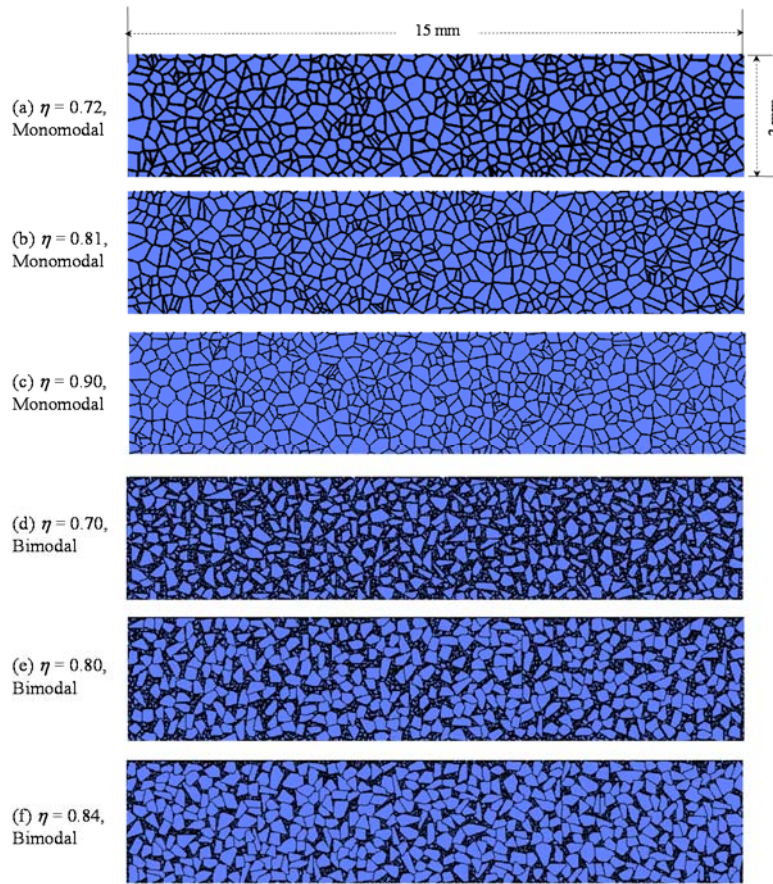


Fig. 14 Examples of microstructures analyzed -- idealized microstructures for PBXs with different grain size distributions and volume fractions, (a) monomodal PBX $\eta = 0.72$, (b) monomodal PBX $\eta = 0.81$, (c) monomodal PBX $\eta = 0.90$, (d) bimodal PBX $\eta = 0.70$, (e) bimodal PBX $\eta = 0.80$, and (f) bimodal PBX $\eta = 0.84$

We have developed a capability to generate large number(>1000) of microstructures using Voronoi tessellation function, which allows their microstructural attributes to conform to prescribed statistical distribution functions, averages and random fluctuations in a controlled

manner. Twenty statistically similar microstructures are generated for each type of microstructural attributes, yielding total 120 (20 x 6) microstructures. Figure 15 shows microstructures having the same volume fraction of $\eta = 0.81$ and monomodal grain size distribution, but random variations in morphology.

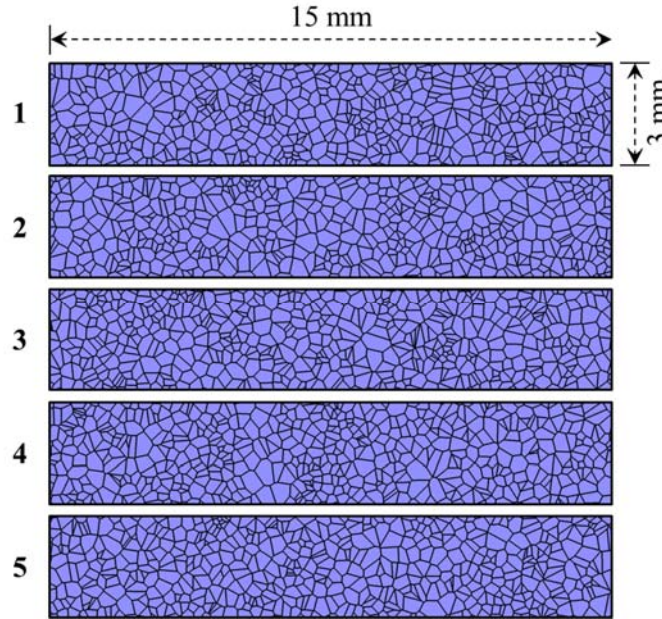


Fig. 15 Examples of statistically similar microstructures – monomodal PBX with $\eta = 0.81$ (only 5 examples among 20 microstructures are shown.)

The stochastic behavior of ignition time is systematically analyzed for microstructures with different volume fractions ($\eta = 0.72\text{--}0.90$) and grain size distributions (monomodal, bimodal) as shown in Fig. 14. Figures 16(a-f) show the probability distributions of the time to criticality t_c for all types of microstructural configurations over the range of impact velocity of 100 – 250 m/s. Major findings from this analysis are :

- (1) Effect of grain volume fraction : The distributions of times to criticality for the lower volume fractions are over wider ranges compared with the distributions for the corresponding higher grain volume fractions.
- (2) Effect of impact velocity : The distribution of time to criticality is more spread out at lower impact velocities, because hotspots are more spatially spread out and more significantly influenced by random material heterogeneities. At high impact velocities, dissipation and heating are the most intense near the impact face, resulting in concentrated hotspots. Consequently, times to criticality for hotspots vary less among different samples.
- (3) Effect of bimodal and monomodal grain size distribution : The time to criticality is more spread out for bimodal microstructures than for monomodal microstructures at the same packing density and the same load intensity, because smaller grains in microstructures with bimodal grain size distributions can rearrange and more effectively absorb the loading to

keep stresses and temperature rises lower, leading to longer times to criticality and larger variations among samples in each set.

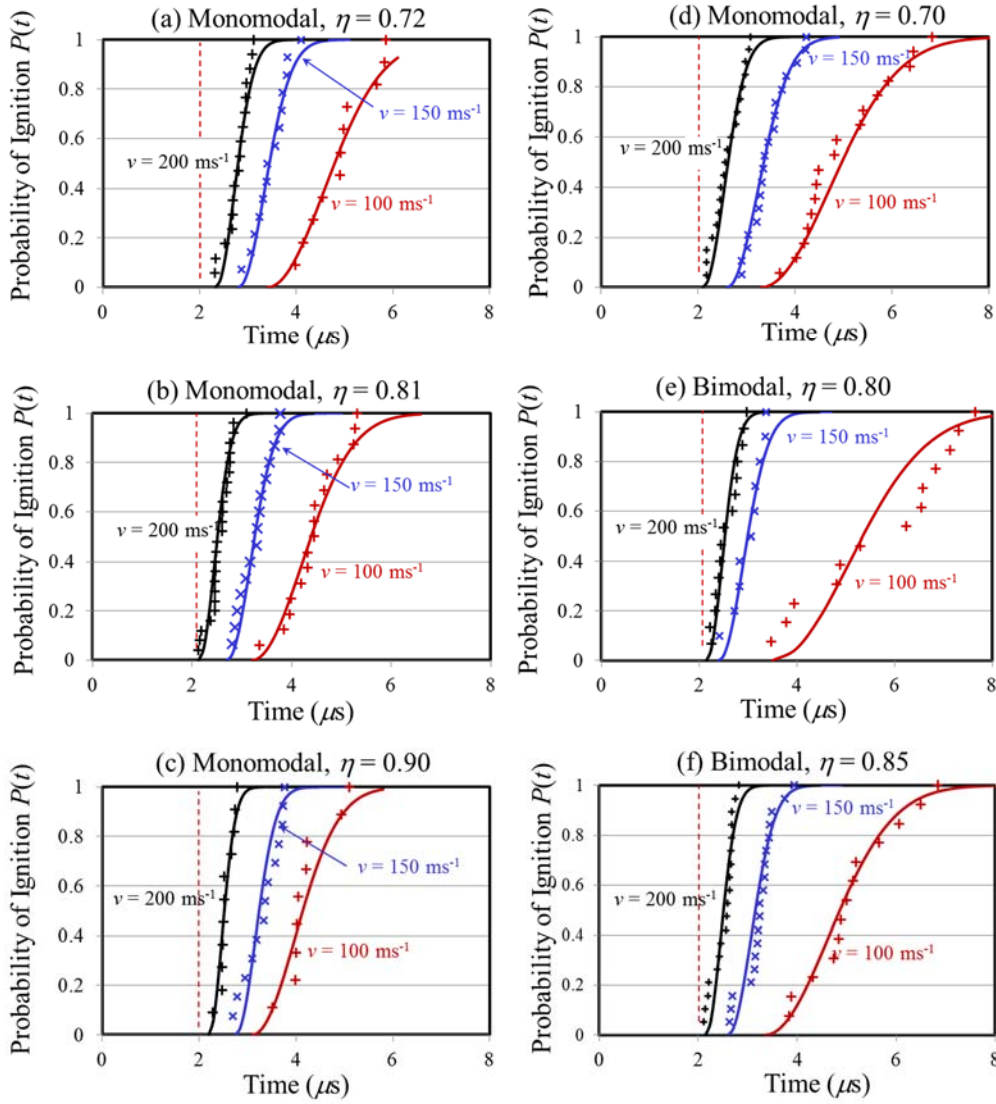


Fig. 16 probability distributions of the time to criticality for microstructures with different grain volume fractions ($\eta = 0.72-0.90$) and grain size distributions (monomodal and bimodal) for impact velocity $v = 100-250$ m/s.

- (4) Effect of variation of grain size distribution: Ignition probabilities from two sets of microstructures are compared, one with large and the other with small variations in grain size distributions among samples in a given microstructure set (monomodal PBX $\eta = 0.81$) as shown in Fig. 17. At a lower velocity of $v = 100$ m/s, the ignition probability from the two sets show similar behavior at the low end of the curves but diverge at the high end of the curves, as presented in Fig. 18(a). Specifically, the set with large variations in grain size distributions has a steeper profile and less variation in response than the set with smaller variations in grain size distributions, which is inconsistent with the logically expected trend. The result suggests that the samples in the two sets of microstructures are

not sufficiently similar in a statistical sense. In other words, simply having the same packing density, average grain size and average grain size distribution is not sufficient to guarantee statistical similitude of microstructures when it comes to impact-induced ignition of PBXs.

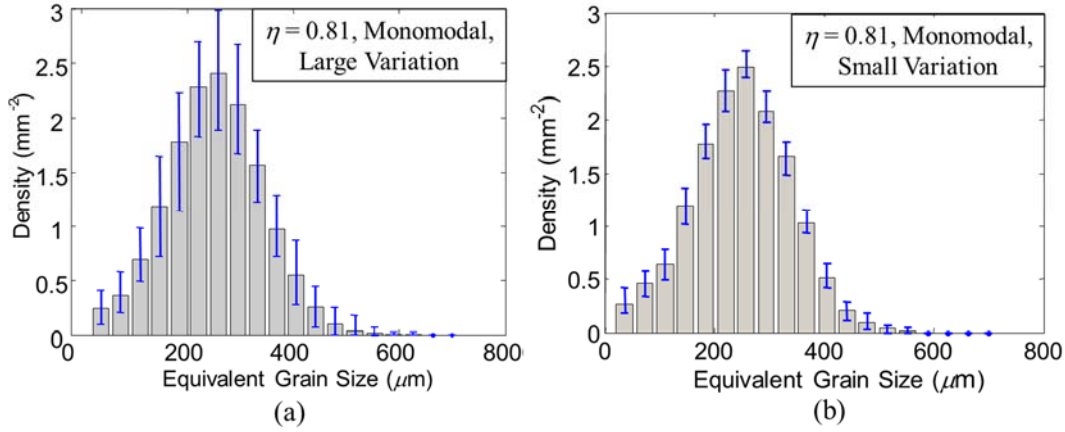


Fig. 17 Grain size distributions for microstructures having the same grain volume fraction of $\eta = 0.81$ with (a) large grain size distribution variations and (b) small grain size distribution variations about the mean grain size distribution.

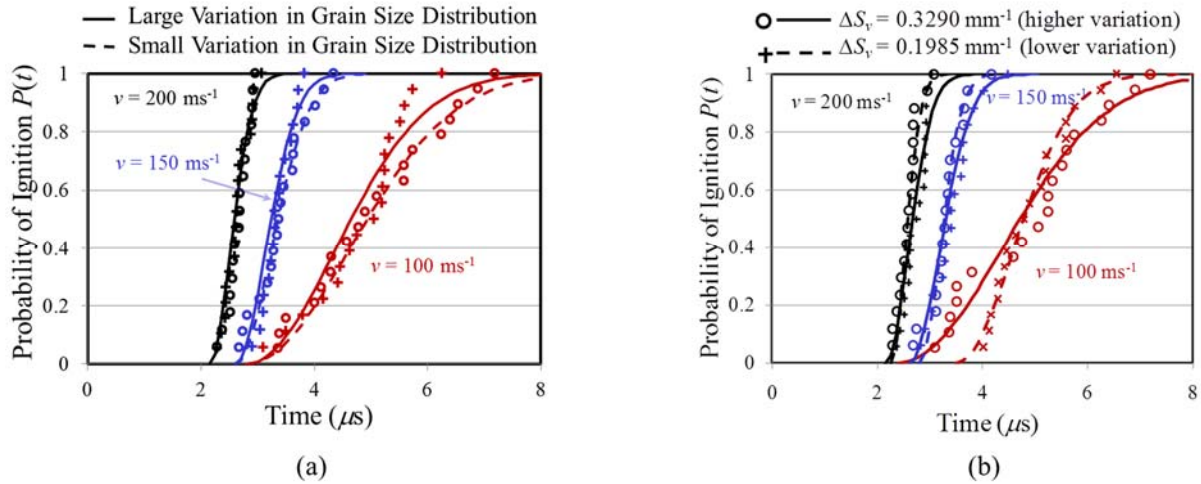


Fig. 18 probability distributions of the time to criticality for (a) microstructures with different levels of variations in grain size distributions, and for (b) microstructures with different variations in interface area per unit volume. Both cases have volume fraction of $\eta = 0.81$

- (5) Effect of statistical variation of specific surface area (ΔS_v) : Ignition probabilities from two sets of microstructures are compared, one with large and the other with small variations of specific surface area (ΔS_v). The results in Fig. 18(b) show that higher values of ΔS_v correspond to higher spreads in the time to criticality. The difference in the spread of data increases as the impact velocity decreases. This shows that the variations in microstructures can be reasonably well quantified by ΔS_v in the context of impact-induced ignition of PBXs.

The probability of ignition time is fitted to a modified Weibull distribution function with a lower threshold time of the form

$$P(t) = 1 - e^{-\Phi(t)}, \quad \Phi(t) = \begin{cases} 0, & t < t_0 \\ \left(\frac{t-t_0}{\tau}\right)^m, & t \geq t_0 \end{cases} \quad (1)$$

where t is the time to criticality, t_0 is the cutoff or threshold time below which the probability of ignition is zero, τ is a scale parameter which affects the slope of the distribution curve, and m is a shape parameter. We have found the relation between mathematical Weibull model and physical process of ignition probability. The effect of impact velocity on each Weibull parameter is also investigated.

- (6) Physical basis for Weibull distribution model : Terao's approach to modeling ignition [8] in gases lends itself to the modeling of impact-induced ignition in solid high explosives. The ignition probability per unit volume per unit time is

$$\mu(t) = -\frac{1}{V} \frac{d[\ln(1-P)]}{dt}, \quad (2)$$

where μ corresponds to the probability of collision and subsequent reaction between molecules in Terao's model. A functional form of $\mu(t)V(t)$ is obtained by two sets of numerical tests, one with impact loading involving wave propagation throughout the domain, and the other with uniform loading involving no stress wave propagation. The uniform loading condition uses a linearly distributed initial velocity field with $v =$ the imposed boundary velocity at $x = 0$ and $v = 0$ at $x = 3$ mm. Eq. (3) is obtained from the results presented in Fig. 19 by using power-law function, which is equivalent to Weibull distribution shown in Eq. (1)

$$\int_0^t \mu(t)V(t)dt = -\ln[1-P(t)] = \left(\frac{t-t_0}{\tau}\right)^m \quad (3)$$

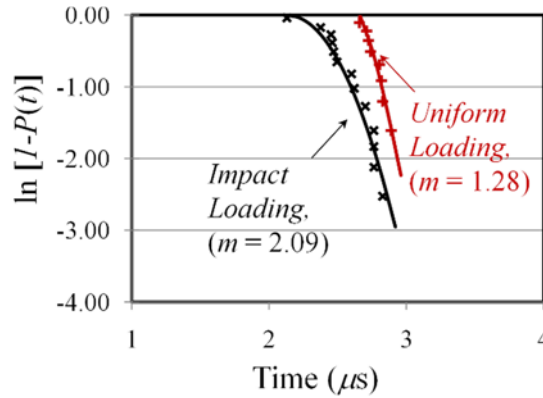


Fig. 19 Probability of ignition time of uniform loading and impact loading (monomodal, $\eta = 0.81$, $v = 200$ m/s).

- (7) Effect of loading condition on shape parameter (m) : Eq. (3) indicates that $m = 1$ means $\mu(t)V(t)$ being constant in terms of time, and $m = 2$ means $\mu(t)V(t)$ being linear function of time. As presented in Fig. 19, for the uniformly loaded case, $m = 1.28 > 1$, reflecting that fact that the temperature, and therefore the probability for ignition increases as the loading event progresses. For the impact loading case with wave propagation, $m = 2.09$, signifying a higher rate of increase of the probability for ignition resulting from the combined effects of increasing temperature and increasing volume of material involved. This value is close to the theoretical value of $m = 2$ for the special case with $\mu(t)$ being constant behind the propagating wave front.

For impact loading, m value does not change with microstructural attributes(monomodal and bimodal, $\eta = 0.70$ – 0.90) or impact velocities($v = 100$ – 250 m/s) as presented in Fig. 20, implying that m is primarily dependent on the loading configuration and is not significantly influenced by microstructure or loading intensity.

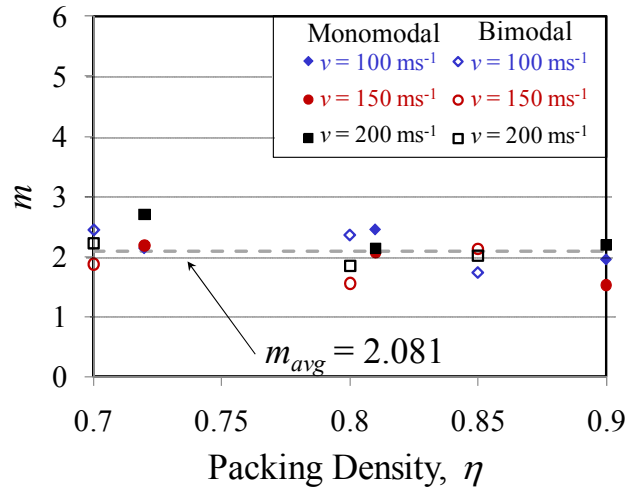


Fig. 20 Probability of ignition time of uniform loading and impact loading (monomodal, $\eta = 0.81$, $v = 200$ m/s).

- (8) Effect of impact velocity (v) on threshold time (t_0) : For both monomodal and bimodal microstructures, as the boundary velocity increases, the threshold time t_0 decreases. This is expected since an increase in impact velocity leads to earlier fracture and frictional dissipation in the grains. This in turn, results in earlier formation of critical hotspots.
- (9) Effect of microstructure and impact velocity(v) on scaling parameter(τ) : τ varies with both microstructure and load intensity as presented in Fig. 21. For all microstructures, τ decreases (and $1/\tau$ increases) as the impact velocity increases. A higher τ implies a wider range of distribution of t_c . At the same impact velocity, τ decreases as the grain volume fraction increases, indicating that the probability distribution of t_c narrows to a shorter time range.

(10) Effect of microstructure on threshold velocity v_c : A value of $\tau = \infty$ ($1/\tau = 0$) indicates that the probability of ignition is zero. The velocity at which zero probability occurs (v_c) can be determined by extrapolating the curves in Figs. 21(a-b) to the horizontal axis. The threshold velocity (v_c) decreases as the grain volume fraction increases as shown in Fig. 22. The threshold velocity (v_c) can be expressed as a function of the grain volume fraction and the specific interface area in the form of

$$v_c(\eta, S_v) = v_0 \eta^{-1.2} \left(1 + \frac{S_v}{S_0} \right)^{0.3} . \quad (4)$$

The threshold velocity (v_c) using Eq. (4) is consistent with experimental data performed by Chidester *et al.*[9] and Gruau *et al.*[10].

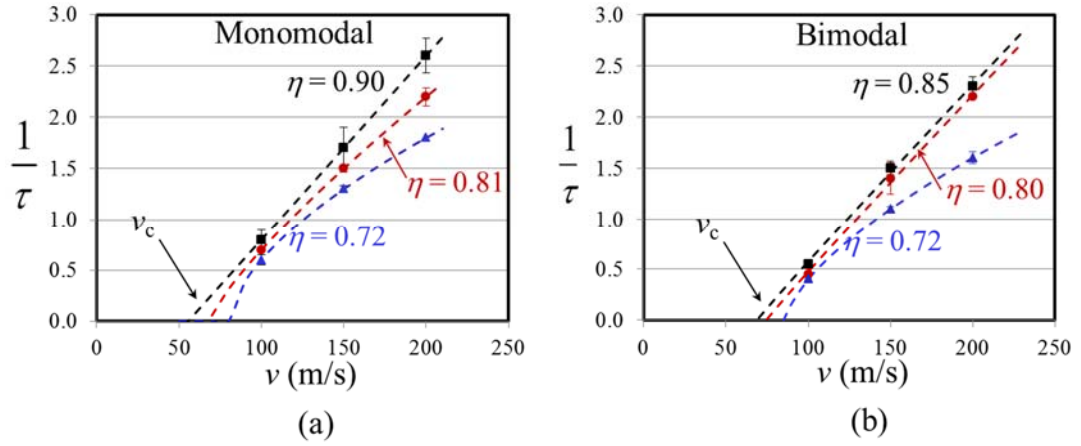


Fig. 21 Scaling parameter τ as a function of impact velocity for microstructures with a range of grain volume fractions ($\eta = 0.72-0.90$), (a) monomodal and (b) bimodal grain size distributions.

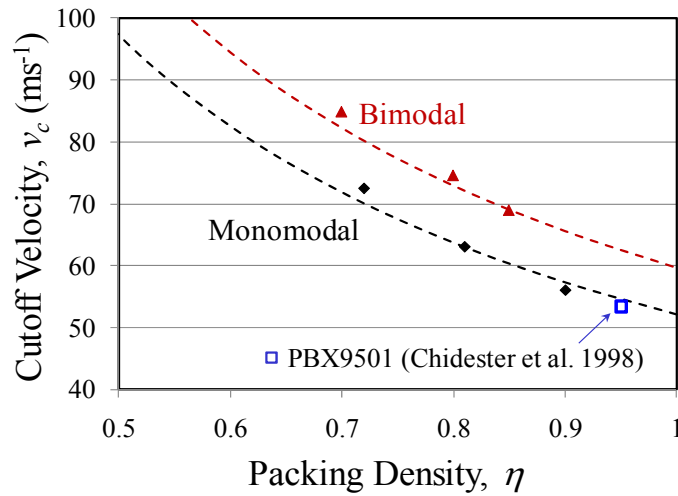


Fig. 22 Comparison of experimental threshold velocity v_c for PBX9501 (Chidester et al.) and numerically predicted values as a function of grain volume fraction ($\eta = 0.70 - 0.90$) and grain size distributions (monomodal, bimodal).

Quantification of the Ignition Probability as a Function of Random Variations in Microstructural Morphology and Inter-constituent Bonding

Computationally Generated Microstructures with Realistic Morphologies:

To obtain microstructures that are similar to PBX9501, we use a grain library with a bimodal grain size distribution. This library consists of grains extracted from microstructures generated by the Voronoi tessellation method. Two microstructures, one with large grains and the other with small grains, are generated. The grains in each microstructure are detected and stored separately in the grain library. Finally, grains in the library are randomly distributed on the microstructure domain as seen in Fig. 23(a).

The evaluation of the computationally generated microstructure is performed by comparing the two-point correlation function of PBX 9501 [11] microstructure and that of computationally generated microstructure. Figure 23(b) shows that the two-point correlation function of PBX 9501 microstructure strongly matches that of the computationally generated microstructure from the grain library approach.

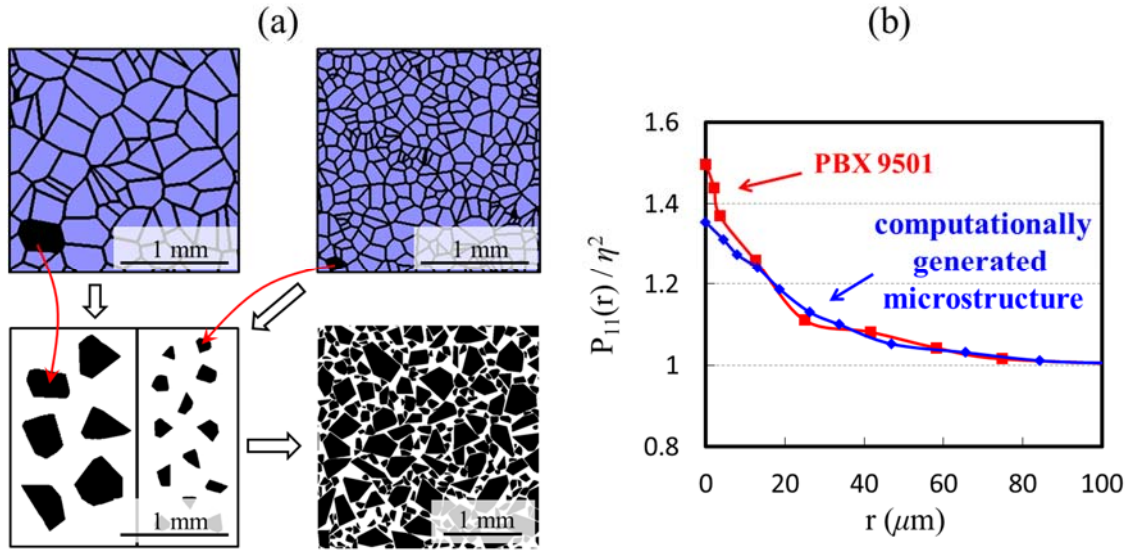


Fig. 23 Computationally generated realistic microstructure; (a) Illustration of microstructure generation using Voronoi tessellation and grain library; (b) Comparison of the two-point correlation functions of the microstructure of PBX 9501 [11] and computationally generated microstructure

Combined Probability From Multiple Sources of Stochasticity:

We analyzed the effects of two sources of stochastic variations at the microstructural level on hotspot development in a PBX. The random variations considered are associated with ① the morphologies of constituent phases and ② the bonding strength of the grain-binder interfaces.

Microstructures with statistically similar properties are generated with variations in the morphologies of the grains and binder [see Fig. 24(a)] and in the interfacial bonding strength between the grains and the binder [see Fig. 24(b)]. The probability of ignition arising from one source of stochastic variation is quantified and analyzed separately from another source. The two probability functions are then combined using relations between the time to criticality and microstructure attributes.

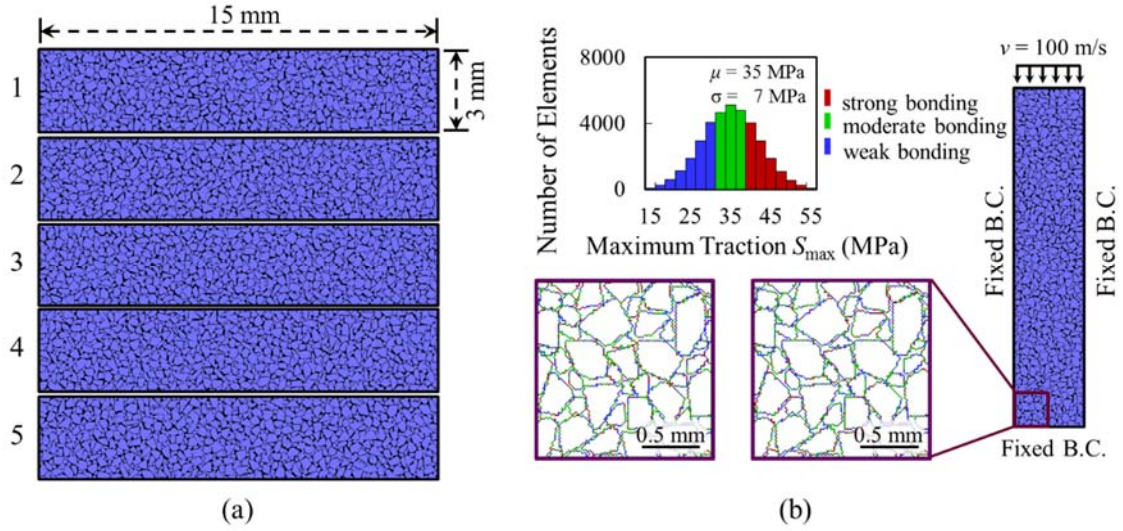


Fig. 24 Microstructures with two sources of stochasticity; (a) stochastic variations in morphologies of constituent phases; (b) stochastic variations in bonding strength of the grain-binder interfaces

Hotspot field quantities are analyzed for microstructures with the variations in morphology. Two parameters, hotspot number density and hotspot area fraction are quantified, and related to the ignition. Results show that more hotspot quantities (i.e., area fraction and number density of hotspots) are observed from microstructures that ignite earlier time than from those that ignite later time, indicating that the development of hotspots is one factor that determines the ignition sensitivity of the microstructure. It is also found that, as shown in Fig. 25, the overall appearances of hotspot fields for microstructures with variations in bonding strength (Mv) show strong resemblance to those for microstructures of corresponding morphologies with uniform bonding strength. However, peak temperatures of the critical hotspots are different, indicating that the variations in interfacial bonding strength provide a perturbation to the thermo-mechanical processes and cause the temperature development to be different.

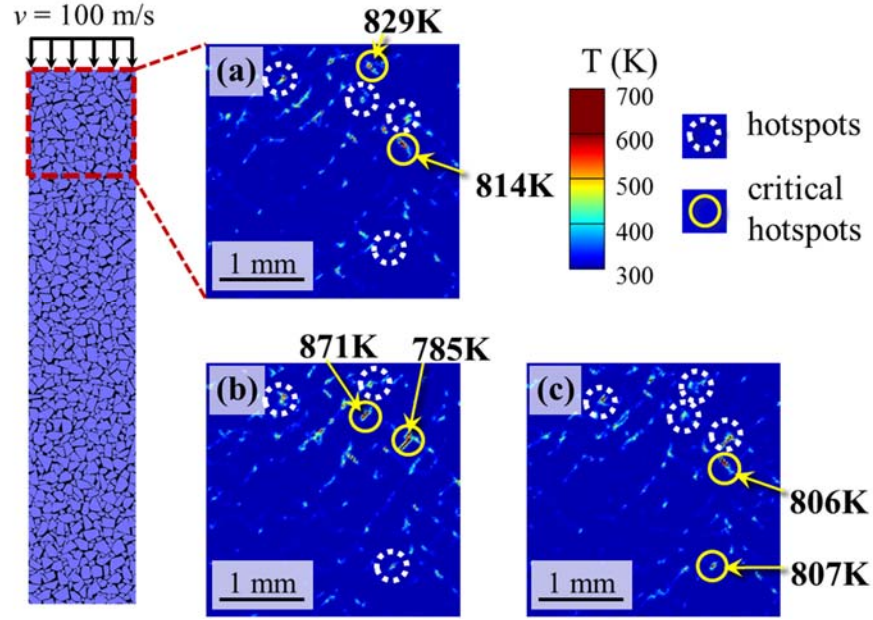


Fig. 25 Temperature field and hotspot locations at $t = 6 \mu\text{s}$ (a) from a microstructure with uniform interfacial strength and (b) and (c) from the same morphology with varying interfacial strength. Circles indicate the hotspots (in white dotted line) and the critical hotspots (in yellow solid line).

The combined effect of two sources of stochasticity - phase morphology changes and variations in interfacial strength - are analyzed. Figure 26(a) shows the probability distribution (Distribution-U) from a microstructure set having the variations in morphology with uniform interfacial strength (M_U). Among a set of microstructures with the variations in morphology having uniform interfacial strength of 35 MPa, three microstructures are chosen as examples for this analysis. The first microstructure, referred to as $\{A\}$, yields the earliest time to criticality $t_c\{A\}$; the second microstructure, referred to as $\{B\}$, yields the median time to criticality $t_c\{B\}$; and the third microstructure chosen, referred to as $\{C\}$, yields the longest time to criticality $t_c\{C\}$ among the twenty samples. Now, these three samples are used to generate three new sets of samples, each based on one of the three original samples. These three new sets, each consisting of twenty samples, constitute a total of 60 samples. The samples in each set have the same microstructure morphology as the corresponding one among the three representative microstructures chosen (A, B, or C), but have binder-grain bonding strengths that vary randomly from location to location.

Figure 26(b) shows the probability of ignition as a function of time for the three new sets of microstructures. The term “Distribution-V” refers to the probability distribution of the time to criticality arising from the random fluctuations in interfacial strength only. Two interesting features are observed when the Distribution-V’s are compared with their baseline ignition times $t_c\{A\}$, $t_c\{B\}$, and $t_c\{C\}$ in Distribution-U. The first feature is that the baseline ignition time ($t_c\{A\}$, $t_c\{B\}$, and $t_c\{C\}$) in Distribution-U (Fig. 26(a)) is not the mean ignition time for the corresponding sample sets giving rise to Distribution-V. Specifically, for microstructure morphology $\{A\}$ which has the shortest ignition time $t_c\{A\}$, the corresponding ignition times in Distribution-V are mostly

later than $t_c\{A\}$ [note the dotted vertical line in Fig. 26(b)]. On the other hand, the opposite is observed for microstructure morphology $\{C\}$ which has the longest ignition time $t_c\{C\}$ —the corresponding ignition times in Distribution-V are mostly earlier. For microstructure morphology $\{B\}$, the corresponding ignition times in Distribution-V straddle both sides of $t_c\{B\}$.

The second feature is that the ranking order of mean ignition time of Distribution-V's for the three new sample sets follow the same order of the ignition time for the three baseline microstructures in Distribution-U, i.e., $t_c\{A\}$, $t_c\{B\}$, and $t_c\{C\}$. As discussed above, the hotspot locations in the microstructures with uniform interfacial strength are similar to the hotspot locations in the corresponding microstructures with random fluctuations in interfacial strength around the uniform strength value, as seen in Figs. 25(a-c). The similarity in hotspot locations shows that sites for the occurrence of dominant hotspots are primarily determined by microstructure morphology and material heterogeneity. In contrast, fluctuations in interfacial strength cause stochastic field (e.g., temperature) perturbations that “modulate” the degree of localization of the field quantities. As a result, variations in interfacial strength cause stochastic variations in ignition time relative to the ignition time determined by the material heterogeneity inherent in the microstructures.

The dependency of Distribution-V on Distribution-U is quantified using three-parameter Weibull distribution functions. The median time to criticality (t_{50}) and the time-scale parameter (τ) to capture the overall shift of the distribution with respect to time and the slope of the distribution. The relations are represented by

$$\frac{t_{50,V}}{t_{50,U}} = \alpha \left(\frac{t_{C,U} - t_{50,U}}{t_{50,U}} \right) + \beta, \text{ and } \frac{\tau_V}{\tau_U} = \gamma \left(\frac{t_{C,U} - t_{0,U}}{\tau_U} \right) + \delta, \quad (5)$$

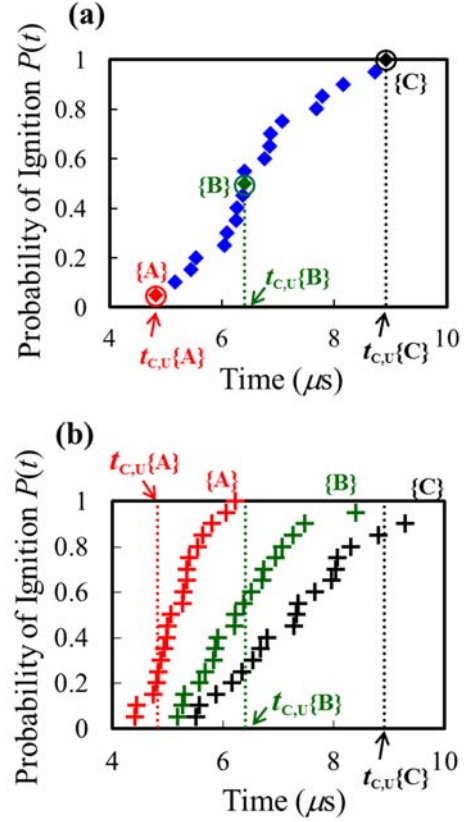


Fig. 26 Relation between Distribution-V and the ignition time of the corresponding MU; (a) Distribution-U; (b) Distribution-V's from the selected microstructure morphologies, $\{A\}$, $\{B\}$, and $\{C\}$. The dotted vertical lines represent the ignition times of corresponding MU in Fig. 26(a).

where α , β , γ , and δ are fitting constants. Here, subscript “U” denotes the value obtained from Distribution-U, and subscript “V” denotes the value obtained Distribution-V.

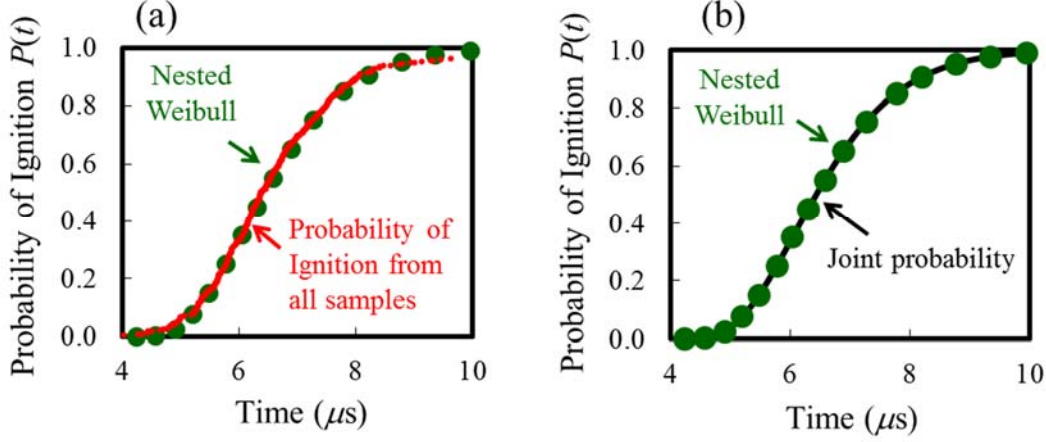


Fig. 27 Combined probability distributions; (a) Comparison between Nested Weibull distribution (green dots) and the probability distribution data from all samples (red line); (b) Comparison between nested Weibull distribution (green dots) and the Joint probability function (black line).

To understand how the different sources combine to affect the overall ignition behavior, we propose a nested probability superposition model based on the relation between Distribution-V on Distribution-U. This nested probability model recognizes the fact that there are “two layers” of probability distributions. The first layer is due to random variations in microstructure morphology. The second layer is associated with the fluctuations in interfacial bonding strength. Ultimately, the nested ignition probability function must agree with the total ignition probability distribution obtained with all cases which are considered as a statistical ensemble of one sample set. Figure 27(a) shows the combined distribution function obtained by using the nested probability (green dots) and the probability distribution of time to criticality represented by all 400 samples (red line). The probability of ignition for an arbitrary sample among a statistical ensemble of all samples is mathematically known as the joint probability of two probability functions—a conditional probability function of Distribution-V and a probability function for Distribution-U. The equation form is

$$p(t) = \int_{t_{C,U}=t_{0,mor}}^{\infty} \left[H(t-t_{0,i}) \cdot \frac{2}{\tau_i} \left(\frac{t-t_{0,i}}{\tau_i} \right) \cdot \exp \left\{ - \left(\frac{t-t_{0,i}}{\tau_i} \right)^2 \right\} \cdot \frac{2}{\tau_U} \left(\frac{t_{C,U}-t_{0,U}}{\tau_U} \right) \cdot \exp \left\{ - \left(\frac{t_{C,U}-t_{0,U}}{\tau_U} \right)^2 \right\} \right] dt_{C,U}, \quad (6)$$

where τ_U and $t_{0,U}$ are $t_{0,V}$ and τ_V as obtained from Eq. (5). Figure 27(b) shows the analytical function of joint probability [shown in black line], and the nested Weibull function [shown in green dots]. The distributions from the two approaches provide identical results, confirming that

Joint probability is the analytical form of the nested Weibull distribution.

Quantification of the Effect of Viscoplasticity on Ignition Sensitivity

We have implemented an elastic-viscoplastic constitutive relation for the HMX particles, and quantified the effect of viscoplasticity on ignition sensitivity of HMX/Estane PBX. A detailed description of the model can be found in [12]. The parameters for the viscoplasticity model have been calibrated to match the experimental wave structure seen in [13]. Figure 28 **Error! Reference source not found.** shows the comparison between the computational material fit and the experimental data.

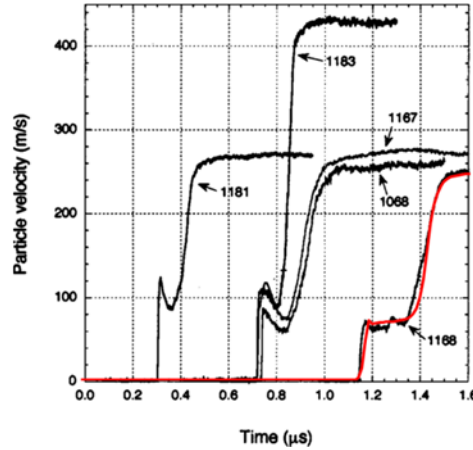


Fig. 28 Comparison of experimental (black) and numerical wave structure (red) resulting from the impact of solid HMX. (Figure from Dick et al.[13]).

The stochastic behavior of ignition time is systematically analyzed for microstructures with different volume fractions ($\eta = 0.72\text{--}0.90$) and HMX material descriptions (hyperelastic and elastic-viscoplastic). Figure 29(a-f) shows the probability distributions of the time to criticality t_c for all types of configurations over the range of impact velocity of 100 – 200 m/s.

Effect of elastic-viscoplastic behavior in HMX:

Accounting for elastic-viscoplastic deformation in HMX has three significant effects on the ignition sensitivity behavior of PBX. (1) Viscoplastic deformation in the HMX phase induces a reduction in time to criticality. (2) The spread of critical times to ignition increases with viscoplasticity. (3) Viscoplasticity intensifies the effect of packing fraction on time to criticality. Effect (3) indicates that the elastic-viscoplastic material behavior in the HMX is more effective at distinguishing between microstructures containing different amounts of HMX.

The vertical dashed lines in Fig. 29 correspond to the earliest time for which any microstructure contains a critical hotspot. This figure shows that the microstructures with elastic-viscoplastic HMX not only have earlier ignition threshold times than the purely elastic microstructures, but the viscoplastic specimens also tend to have later maximum ignition times. This effect indicates again

that the viscoplastic deformation magnifies the effect of microstructure on the ignition sensitivity in PBX specimens.

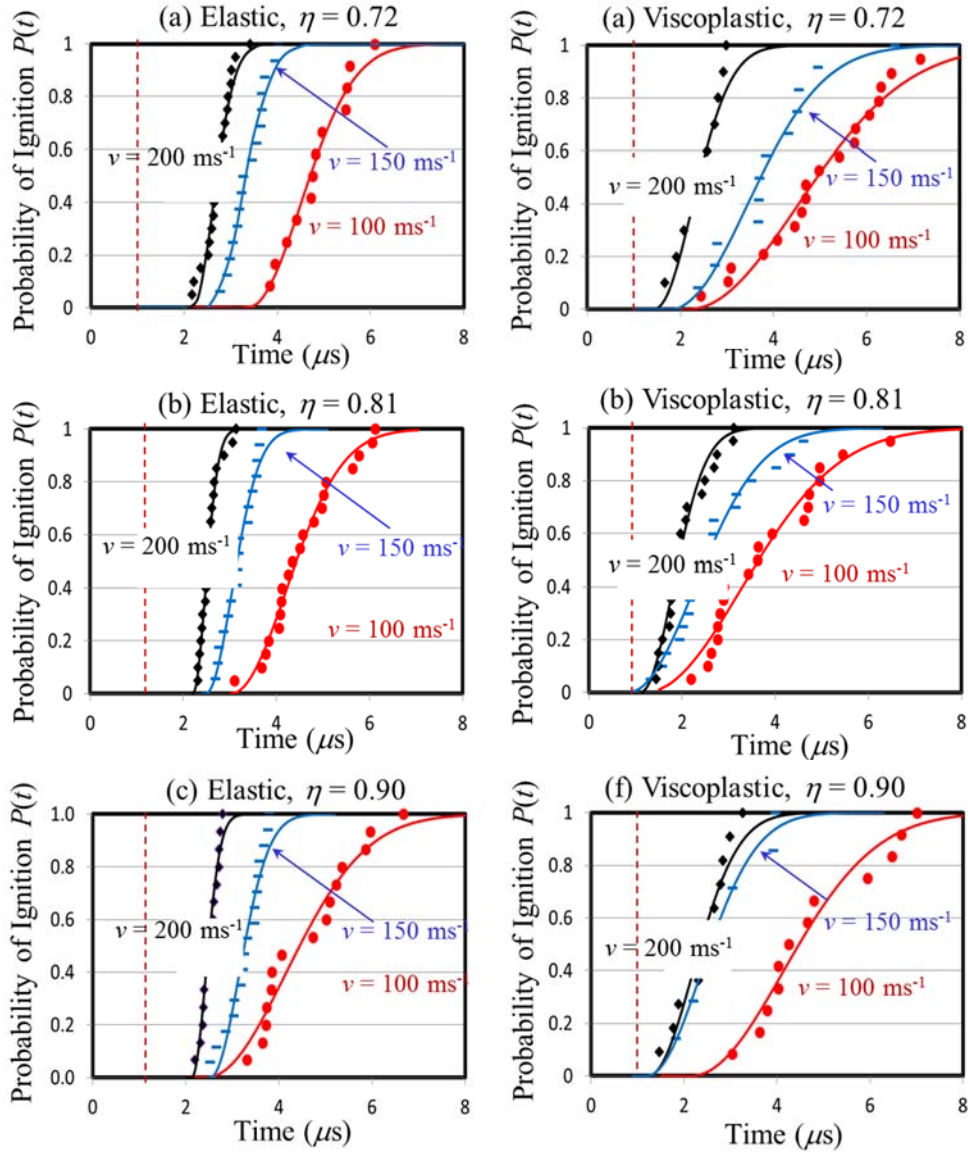


Fig. 29 Probability distributions of the time to criticality for microstructures with different grain volume fractions ($\eta = 0.72\text{--}0.90$) and HMX material behavior (elastic and elastic-viscoplastic) for impact velocity $v = 100\text{--}200$ m/s.

Major findings from this analysis are :

(1) Effect of piston velocity (v) on threshold time (t_0) :

The threshold time to ignition (t_0) is affected by both the piston velocity and the material behavior of the HMX. Figure 30 shows that the higher piston velocities lead to reduced

effect of packing fraction on the ignition response. For all packing fractions, viscoplasticity in the HMX lowers the initiation threshold by 1.2 – 1.8 μ s for an impact velocity of 100 m/s and 1.1 μ s for 200 m/s.

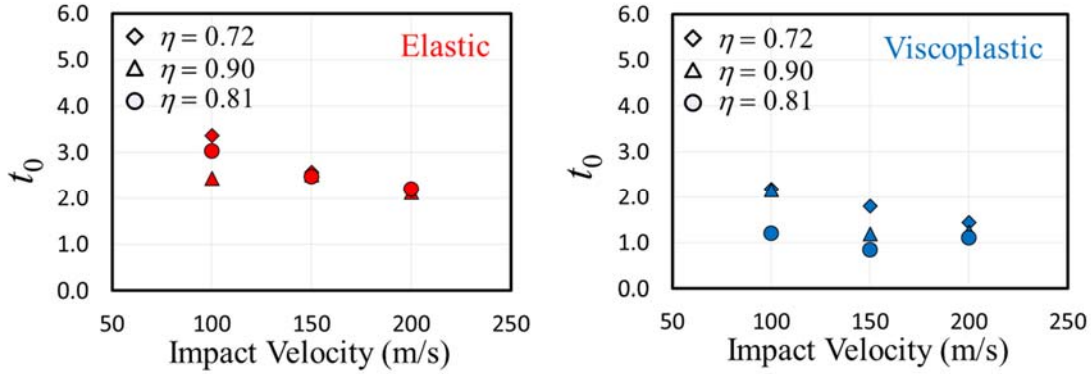


Fig. 30 The effect of HMX material behavior (elastic and elastic-viscoplastic) on t_0 for piston speeds from 100 – 200 m/s and packing fractions of 0.72, 0.81, and 0.90.

(2) Effect of microstructure and impact velocity (v) on t_{50} :

For Weibull distributions of the form used in this work, t_{50} is defined as the time for which the probability that a randomly selected specimen has ignited is 0.5, the mean ignition time. As a measure of ignition sensitivity, it is more convenient than t_0 for measuring and representing the behavior of the entire set of microstructures. Because the mean time to ignition is not sensitive to the extreme ignition cases, it requires fewer microstructural instantiations to reliably obtain. The mean time to ignition decreases monotonically as a function of piston velocity. Specimens with viscoplastic HMX generally have lower mean critical ignition times than the corresponding microstructures with elastically deforming HMX. The one exception is $\eta = 0.72$. For this packing fraction, the viscoplastic specimens are slower to initiate at low velocities and faster at high velocities.

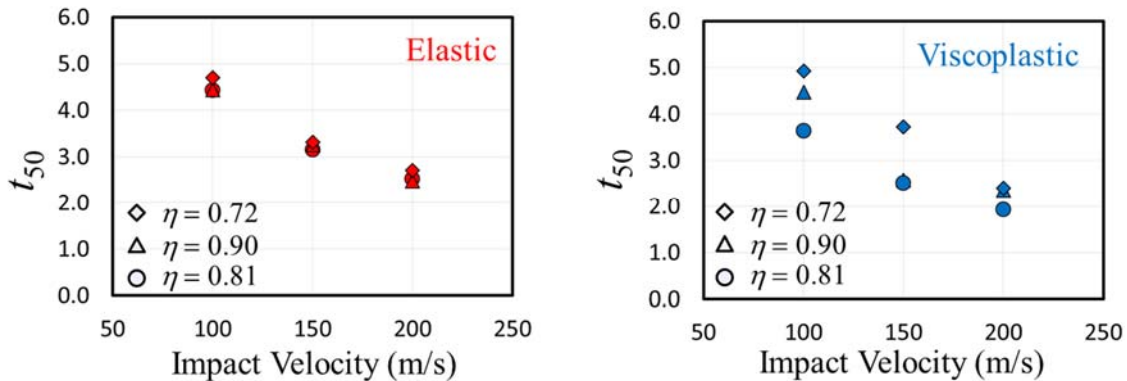


Fig. 31 The effect of HMX material behavior (elastic and elastic-viscoplastic) on t_{50} for piston speeds from 100 – 200 m/s and packing fractions of 0.72, 0.81, and 0.90.

(3) Effect of microstructure and impact velocity (v) on t_{range} :

The range of probable ignition times (t_{range}) is defined here as the time between the ignition threshold time (t_0) and the time when the probability of ignition reaches 99%. This measure is related to τ , but provides a physical frame of reference for the results where τ is a wholly abstract representation. t_{range} is between 42 and 225 % higher in specimens with viscoplastic HMX. Similarly to t_0 and t_{50} , the effect of packing fraction is increased in the viscoplastic specimens, indicating an increased microstructural influence.

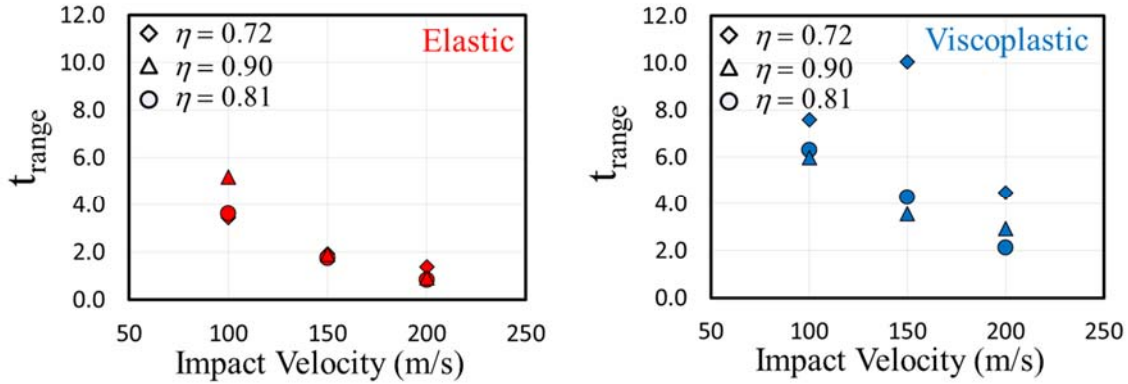


Fig. 32 The effect of HMX material behavior (elastic and elastic-viscoplastic) on t_{range} for piston speeds from 100 – 200 m/s and packing fractions of 0.72, 0.81, and 0.90.

Quantification of Hotspot Generation Rate:

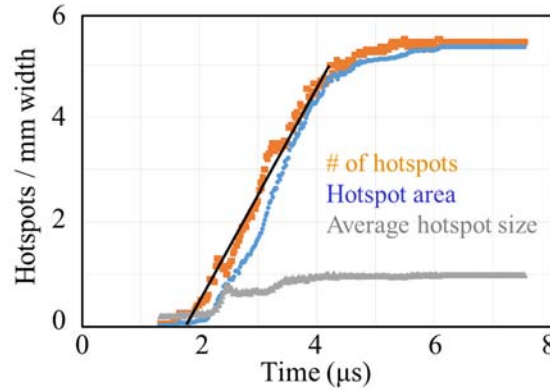


Fig. 33 Total number of hotspots per mm of impact face length in the 20 specimen set having elastic-viscoplastic HMX, $\eta = 0.81$, and 150 m/s piston speed. The slope of the black line is the hotspot generation rate for this set, and the intersection of the black line with the x-axis is the delay time to initiation.

In order to develop a predictive model for the behavior of PBXs under dynamic loads, it is necessary to characterize the hotspot generation rate per unit area of impacted specimen. To approximate a large specimen, the twenty (20) specimens with a 0.81 packing fraction are considered as one wide specimen, and a hotspot is defined as a distinct geometric region with a

temperature in excess of 700 K. Figure 33 shows the evolution of the number of hotspots (orange), total hotspot area (blue), and average hotspot size (grey) for the whole set of specimens.

The evolution of the number density of hotspots in Fig. 33 can be split into three distinct regions: (1) the initial ramp from 0 to 2 μs , (2) the linear region from 2 to 4 μs , and (3) the plateau region above 4 μs . Current focus is restricted to region 2, which is characterized by a nearly constant hotspot generation rate for each microstructural sample set. This region has been fit to a line (black), the slope of which corresponds to the hotspot generation rate for this set of microstructures and the cutoff time is the time corresponding to zero hotspots. Figure 34 shows the hotspot generation rate (red) and the cutoff time (blue) as a function of piston velocity.

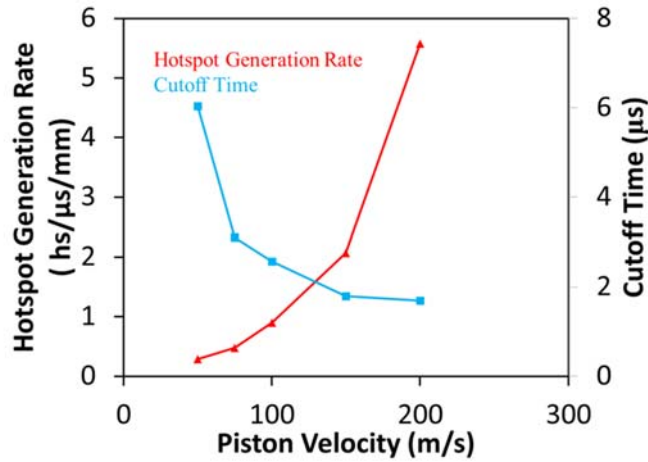


Fig. 34 Hotspot generation rate (red) and cutoff time (blue) as a function of piston velocity for microstructures with a packing fraction of 0.81 and elastic-viscoplastic HMX.

The cutoff time in Fig. 34 indicates that a minimum cutoff time exists at approximately 1.65 μs for hotspots generated due solely to the combined effects of plasticity and frictional heating. This cutoff time does not represent the minimum ignition time. Rather, it is a minimum time for which the PBX specimens are generating hotspots at a constant rate.

Figure 35 shows the distribution of first hotspot locations for each microstructure (measured from the impact surface) as a function of time to criticality for piston velocities from 100 – 200 m/s. For each piston velocity, the location of the first critical hotspot is not significantly influenced by either the material description of the HMX (elastic or elastic-viscoplastic) or the HMX packing fraction.

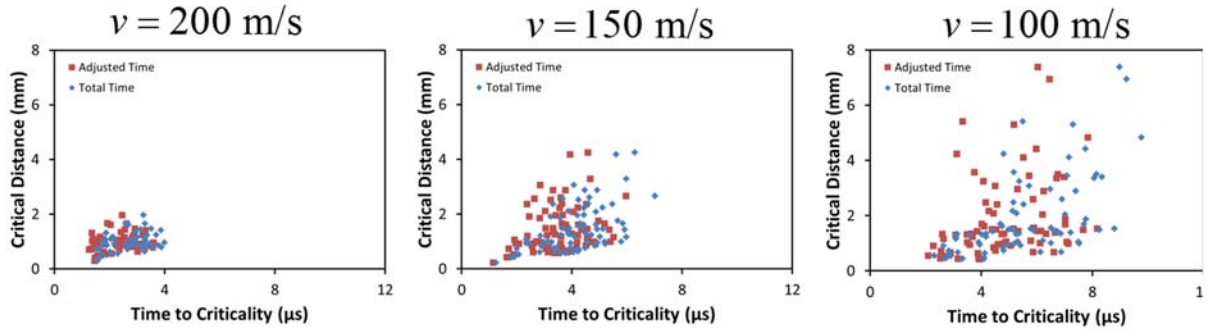


Fig. 35 The space and time distributions of the generation of first critical hotspots in each specimen for piston speeds of 200, 150, and 100 m/s

There is a clear relationship between the piston velocity and the statistical spread of the hotspots in both space and time. The distribution of hotspots generated due to a 200 m/s piston all occur in the range of 1.65 to 4 μs and within the first 2 mm of specimen. When the piston speed is 100 m/s, the distribution of generated hotspots ranges from 2.31 to 9.76 μs and occur in the first 7.4 mm. This result emphasizes that lower velocity impact events greatly enhance the microstructural effect on the ignition sensitivity and hotspot generation in two-phase PBXs.

Ignition Desensitization of PBX via Aluminization

We have analyzed thermomechanical response of aluminized PBX and the corresponding ignition behavior. The microstructures considered are those of a PBX system consisting of either two (HMX/Estane) or three (HMX/Estane/Al) phases. To generate the three-phase system of microstructures, aluminum particles are added to the solid phase of the two-phase (HMX/binder) system. The microstructures are designed in a way to keep the total solid (Al and HMX) fraction constant, while the fraction of the HMX is adjusted accordingly as the Al fraction is increased. The volume fraction of the Al particles is varied from 0% to 18%. Accordingly, the volume fraction of the HMX grains is varied from 81% to 63%, as shown in Fig. 36. Details of the microstructural attributes of the PBX and the method used to generate the microstructure are described in Ref. [14].

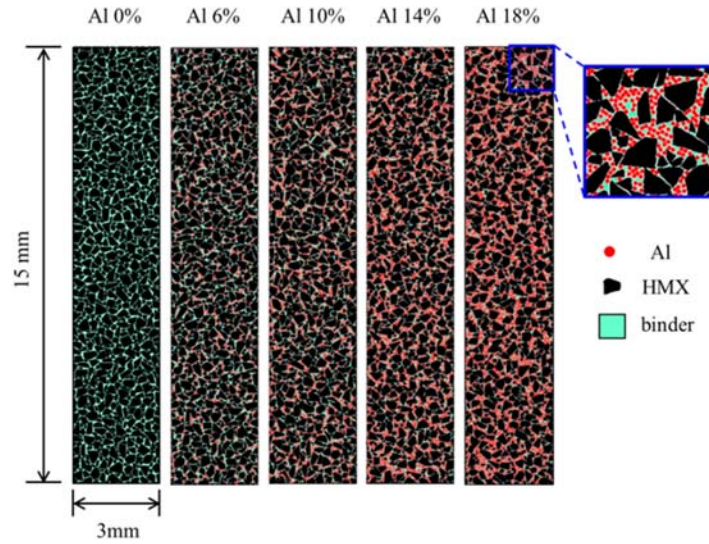


Fig. 36 Microstructures with different Al volume fractions ($\eta_{Al} = 0 - 0.18$) and HMX volume fractions ($\eta_{HMX} = 0.81 - 0.63$). Each image shown represents one sample in a set of twenty statistically similar samples which are random instantiations of the same microstructure condition.

For the aluminized PBX, the stress front shows an elastic precursor, followed by a slower increase which is indicative of plasticity. This effect of plasticity becomes more pronounced as Al content increases. Specifically, the stress histories for cross-sections at $x = 2, 6, 10$ mm are plotted in Fig. 37 for the cases with 0 and 10% Al. The increasing difference between the stress profiles for the unaluminized PBX and the aluminized PBX indicates that, as the stress wave propagates through the material, longer times are required for the aluminized PBX to reach a steady state of stress. The plasticity of Al and the sliding along Al-binder interfaces caused by the addition of the Al particles lead to an overall weakening of the composite material.

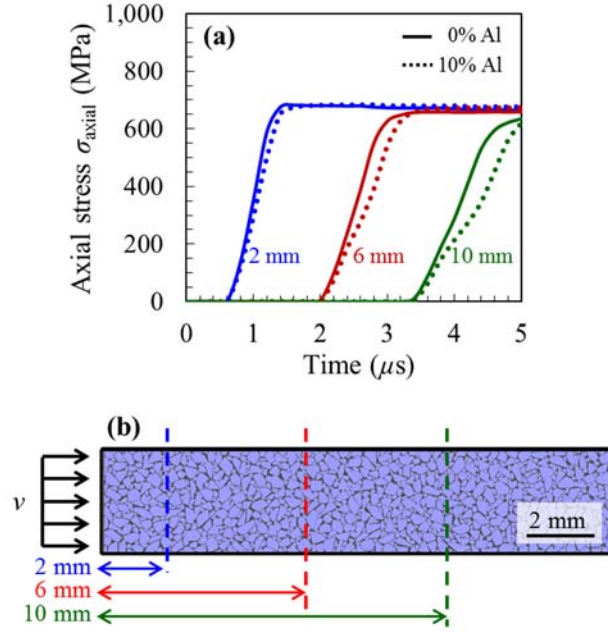


Fig. 37 History of axial stress for unaluminized HMX/Estane PBX (solid line) and aluminized PBX with 10 % Al contents (dotted line) for the locations of $x = 2, 6, 10$ mm.

Dissipation due to fracture and hotspot field characteristics are quantified in the aluminized and unaluminized PBXs. Aluminum particles ($50 \mu\text{m}$ in diameter) are smaller than the smaller group of HMX grains ($123 \mu\text{m}$ average diameter). Therefore, the total sum of surface area of aluminum and HMX granules increases as the aluminum content increases. For this reason, the length density of all cracks increases as the volume fraction of aluminum increases, but the crack density associated with the HMX grains decreases as the volume fraction of aluminum increases, as shown in Fig. 38(a). Figure 38(b) shows the frictional dissipation per unit crack length at cracks associated with the HMX phase. The profile indicates that frictional dissipation at cracks is relatively more intense for the unaluminized HMX/polymer PBXs than for the aluminized PBXs. This difference directly affects the hotspot fields in these materials.

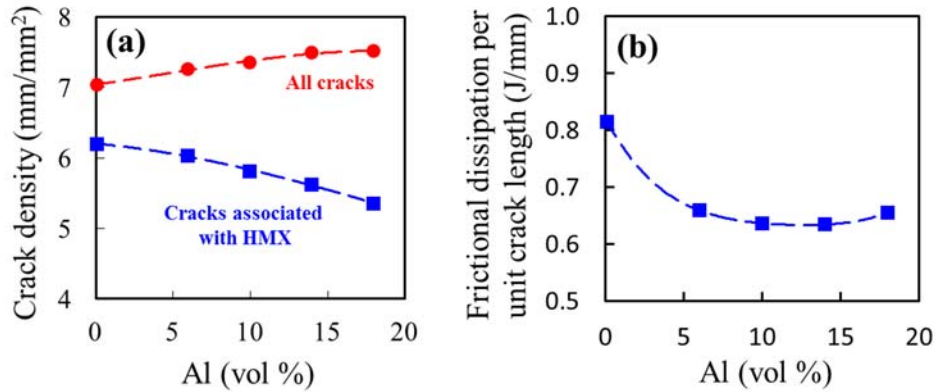


Fig. 38 Effect of Al addition on (a) crack densities and (b) frictional dissipation

Figures 39(a) and (b) show hotspot area fraction and the average hotspot number density, respectively. The addition of aluminum particles significantly decreases the hotspot counts, indicating that the aluminized PBXs are less susceptible to creating hotspots that may result in ignition relative to the unaluminized PBX. Note that frictional dissipation per unit crack length (Fig. 38(b)) shows a trend that is consistent with that of the hotspot counts (Fig. 39). Also, frictional dissipation per unit crack length does not change significantly with the aluminum content over the Al volume fraction range of 10 to 18%, although a significant difference is seen between that for the unaluminized PBX and that for the aluminized PBXs. A similar trend is seen in the hotspot fields as measured by the hotspot area fraction and hotspot density.

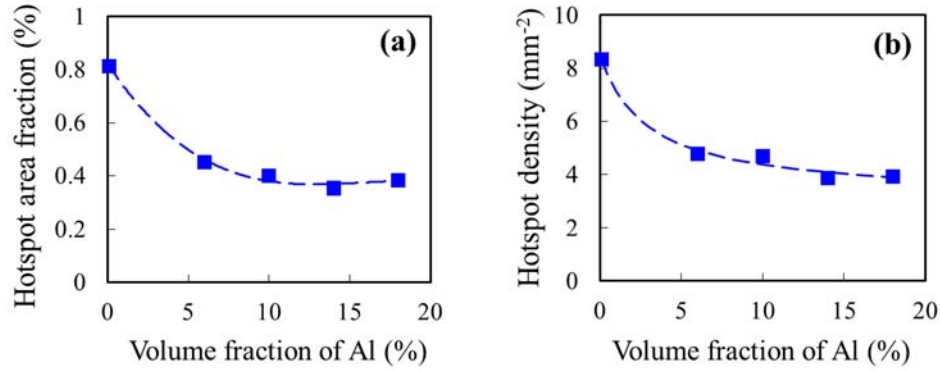


Fig. 39 Effect of Al addition on hotspot counts; (a) hotspot area fraction; (b) hotspot number density

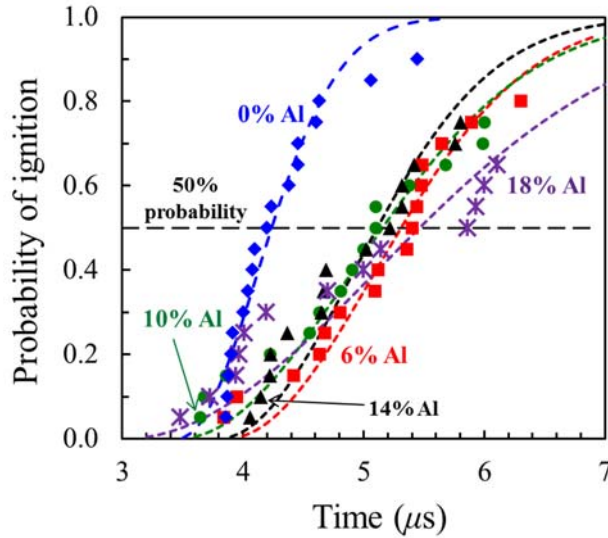


Fig. 40 Ignition probabilities for unaluminized PBX and aluminized PBX with 6 to 18% Al by volume.

The ignition probability shown in Fig. 40 is obtained from the five microstructure sets, each

of which having twenty samples. The PBX without aluminum has relatively earlier ignition times than the aluminized PBXs. This may be interpreted to mean that adding aluminum in PBX makes the material less sensitive in terms of ignition time. In particular, adding Al causes the probability curves to flatten out to the right (longer times), such that the value of mean time to ignition (t_{50}) or the time by which 50% of the samples have reached criticality is higher for higher Al content.

Ignition Behavior of an Aluminum-Bonded Explosives (ABX)

We have studied the potential for a new class of explosives that is based on aluminum and HMX. The proposed composite is comprised of HMX particles suspended in an aluminum matrix, referred to hereafter as ABX or aluminum-bonded explosive. Two types of aluminum are considered, one is commercially provided pure aluminum (Al 1100) and the other one is an aircraft grade aluminum alloy (Al 7075). Compared to the Al 1100, Al 7075 is stronger by a factor of 10 times, but exhibits a lower work hardening rate. Because both types of aluminum have much higher stiffness and shear resistance than polymer, the ABX specimens have noticeably higher axial stresses than PBX specimens under the same piston velocity ($U_p = 200 \text{ m/s}$), as shown in Fig. 41.

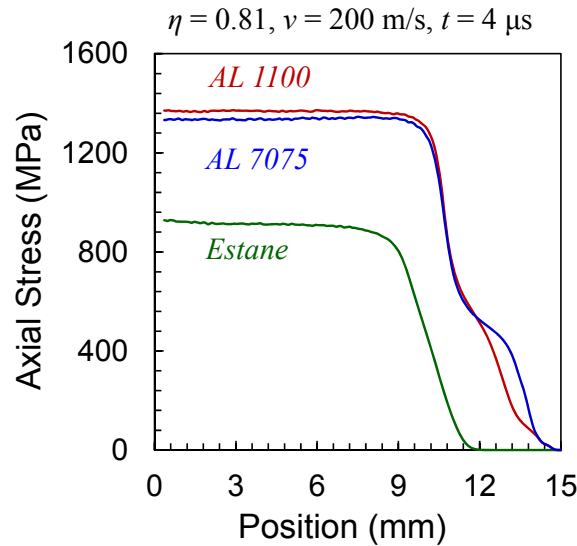


Fig. 41 Axial stress as a function of distance from the piston for various binder systems.

Each of the three microstructure types (① Estane based PBX, ② Al 1100 based ABX, and ③ Al 7075 based ABX) has a pathway to temperature rise that is distinct from the others. ① In the PBX, the vast majority of the heating occurs on the extreme periphery of the grains. The heating in the PBXs concentrate on the grain boundaries because many of the grain boundaries have debonded from the surrounding binder and the grains themselves begin to crack near the edges of the grains. As a result, the region in the vicinity of the grain boundaries has both an abundance of fracture and potential friction sites, as well as more freedom for relative motion due to the proximity to the compliant binder. ② In the weak ABX (Al 1100), no widespread heating is present. In this material, all hotspots come in the form of isolated hotspots of relatively low intensity (compared to those seen in the PBX and strong ABX). The weak ABX composition requires a combination of multiple contributing factors in order to generate a critical hotspot, a fact that likely contributes to the lower observed sensitivity in this material. ③ The strong ABX (Al 7075) heats almost exclusively along a large number of intragranular fractures that occur in

this composition due to the high stiffness of the binder in the vicinity of the stress wave front. For piston velocities incapable of generating large scale cracking in the HMX particles, the heating in the strong ABXs is not sufficient to lead to thermal runaway.

The PBX experiences heating along grain boundaries that have cracks and begin to experience a large magnitude of frictional sliding in the vicinity of the Estane binder which does not have the shear resistance to oppose the sliding. The majority of the heating in the strong ABX (Al 7075 based) takes place in the form of frictional heating along the high density of intragranular cracks nucleated in the HMX grains. For the weak ABX (Al 1100 based), the only appreciable heating observed takes place in regions which combine the heating modes for PBX and the strong ABX. Comparison of the peak temperature rise and frictional dissipation in each of the compositions as shown in Fig. 42 provides an avenue for determining which types of localization characteristics are preferable for decreasing the sensitivity of a composite.

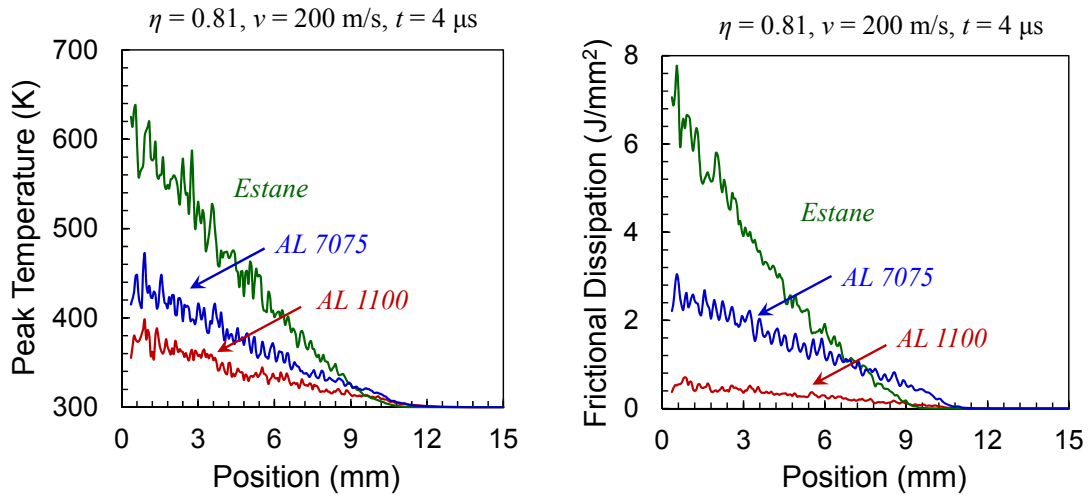


Fig. 42 Peak temperature and frictional heating as a function of distance from the piston for various binder systems.

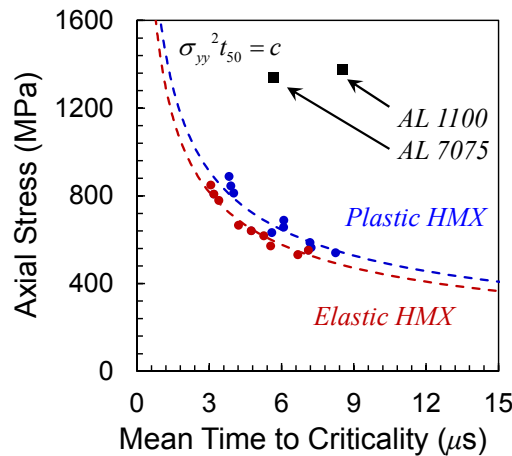


Fig. 43 Comparison of the sensitivity between ABXs and Estane based PBXs

A modification of the relation originally introduced by Walker and Wasley [15] is presented, and fit to the elastic and plastic HMX based PBXs, as shown in Fig. 43. The criticality data points for the two proposed ABX compositions are superimposed in the figure. Both of the ABX compositions are predicted by the preceding analysis to be significantly less sensitive than the associated PBX microstructures. The critical energy corresponding to the fit is 593 kJ/m^2 . By comparison, the calculated critical energy of the strong ABX is 1519 kJ/m^2 and that of the weak ABX is 2336 kJ/m^2 .

References

- [1] Tomar, V., Zhai, J., and Zhou, M., "Bounds for element size in a variable stiffness cohesive finite element model," *International Journal for Numerical Methods in Engineering*, vol. 61, pp. 1894-1920, 2004.
- [2] Rimoli, J. J. and Ortiz, M., "A duality-based method for generating geometric representations of polycrystals," *International Journal for Numerical Methods in Engineering*, vol. 86, pp. 1069-1081, 2011.
- [3] Barton, N. R., Winter, N. W., and Reaugh, J. E., "Defect evolution and pore collapse in crystalline energetic materials," *Modelling and Simulation in Materials Science and Engineering*, vol. 17, p. 035003, 2009.
- [4] Zamiri, A. R. and De, S., "Modeling the Anisotropic Deformation Response of β -HMX Molecular Crystals," *Propellants, Explosives, Pyrotechnics*, vol. 36, pp. 247-251, 2011.
- [5] Baer, M., "Modeling heterogeneous energetic materials at the mesoscale," *Thermochimica acta*, vol. 384, pp. 351-367, 2002.
- [6] Tarver, C. M., Chidester, S. K., and Nichols, A. L., "Critical conditions for impact- and shock-induced hot spots in solid explosives," *Journal of Physical Chemistry*, vol. 100, pp. 5794-5799, Apr 4 1996.
- [7] Barua, A., Kim, S., Horie, Y., and Zhou, M., "Ignition criterion for heterogeneous energetic materials based on hotspot size-temperature threshold," *Journal of Applied Physics*, vol. 113, Feb 14 2013.
- [8] Terao, K., *Irreversible phenomena : ignitions, combustion, and detonation waves*. Berlin ; New York: Springer, 2007.
- [9] Chidester, S. K., Tarver, C. M., and Garza, R., "Low amplitude impact testing and analysis of pristine and aged solid high explosives," in *Eleventh (International) Symposium on Detonation, ONR*, 1998, pp. 33300-5.
- [10] Gruau, C., Picart, D., Belmas, R., Bouton, E., Delmair-Sizes, F., Sabatier, J., and Trumel, H., "Ignition of a confined high explosive under low velocity impact," *International Journal of Impact Engineering*, vol. 36, pp. 537-550, Apr 2009.
- [11] Liu, C., "Specific surface: a missing parameter in high-explosive modeling," LA-14024 United States 10.2172/966982 Tue Oct 13 10:06:57 EDT 2015 LANL English, 2003.
- [12] Zhou, M., Needleman, A., and Clifton, R. J., "Finite-Element Simulations of Shear Localization in Plate Impact," *Journal of the Mechanics and Physics of Solids*, vol. 42, pp. 423-458, Mar 1994.
- [13] Dick, J. J., Hooks, D. E., Menikoff, R., and Martinez, A. R., "Elastic-plastic wave profiles in cyclotetramethylene tetranitramine crystals," *Journal of Applied Physics*, vol. 96, pp. 374-379, Jul 1 2004.
- [14] Kim, S., Barua, A., Horie, Y., and Zhou, M., "Ignition probability of polymer-bonded explosives accounting for multiple sources of material stochasticity," *Journal of Applied Physics*, vol. 115, May 7 2014.
- [15] Walker, F. and Wasley, R., *Critical energy for shock initiation of heterogeneous explosives*: University of California, Lawrence Livermore Laboratory, 1968.
- [16] Landerville, A. C., Conroy, M. W., Budzevich, M. M., Lin, Y., White, C. T., and Oleynik, I. I., "Equations of state for energetic materials from density functional theory with van der Waals, thermal, and zero-point energy corrections," *Applied Physics Letters*, vol. 97, Dec 20 2010.

- [17] Campbell, J. and Vignjevic, R., "Artificial Viscosity Methods for Modelling Shock Wave Propagation," in *Predictive Modeling of Dynamic Processes*, S. Hiermaier, Ed., ed: Springer US, 2009, pp. 349-365.
- [18] Marsh, S. P., *Lasl shock Hugoniot data*. Berkeley: University of California Press, 1980.
- [19] Simpson, R. L., Helm, F. H., and Kury, J. W., "Non-Reactive HMX Shock Hugoniot Data," *Propellants, Explosives, Pyrotechnics*, vol. 18, pp. 150-154, 1993.
- [20] Gresshoff, M. and Hrousis, C. A., "Probabilistic Shock Threshold Criterion," presented at the 14th International Detonation Symposium, Coeur d'Alene, Idaho, 2010.
- [21] Welle, E. J., Molek, C. D., Wixom, R. R., and Samuels, P., "Microstructural effects on the ignition behavior of HMX," *18th Aps-Scem and 24th Airapt, Pts 1-19*, vol. 500, 2014.
- [22] Hudson, R. J., Zioupos, P., and Gill, P. P., "Investigating the Mechanical Properties of RDX Crystals Using Nano-Indentation," *Propellants Explosives Pyrotechnics*, vol. 37, pp. 191-197, Apr 2012.

What opportunities for training and professional development has the project provided?

If the research is not intended to provide training and professional development opportunities or there is nothing significant to report during this reporting period, state "Nothing to Report." Describe opportunities for training and professional development provided to anyone who worked on the project or anyone who was involved in the activities supported by the project. "Training" activities are those in which individuals with advanced professional skills and experience assist others in attaining greater proficiency. Training activities may include, for example, courses or one-on-one work with a mentor. "Professional development" activities result in increased knowledge or skill in one's area of expertise and may include workshops, conferences, seminars, study groups, and individual study. Include participation in conferences, workshops, and seminars not listed under major activities.

1. Graduate student training: the project provided education opportunities for seven PhD students and one master student at Georgia Tech. The seven PhD students are Ananda Barua, David Barrett Hardin, Seokpum Kim, Christopher Michael Miller, Yaochi Wei, Amirreza Keyhani, and Ushasi Roy. Ananda Barua received his PhD degree in May 2013. David Barrett Hardin received his PhD degree in April 2015 and is now a research scientist in the AFRL at the Eglin AFB in Florida. The master student is David Henry Weichsel who received his master's degree in May 2015.
2. Support to Eglin AFB researchers: The project provided several onsite training and support events at Georgia Tech and the Eglin AFB for researchers at the Eglin AFB. The technical aspects of the training are: (a) application and execution of our CODEX software code suites, (b) generation of statistically similar microstructure sets for simulations, and (3) pre- and post-processing of data;
3. User manual, documentation, and material data have been provided to the AFRL at the Eglin AFB; and
4. Seminars and workshops at the Eglin AFB.

How have the results been disseminated to communities of interest?

If there is nothing significant to report during this reporting period, state "Nothing to Report."

Describe how the results have been disseminated to communities of interest. Include any outreach activities that have been undertaken to reach members of communities who are not usually aware of these research activities, for the purpose of enhancing public understanding and increasing interest in learning and careers in science, technology, and the humanities.

Distribution of CODEX

1. The whole suite of our simulation codes (CODEX, which stands for Cohesive Dynamics for eXplosives) as well as extensive pre- and post-processing tools have been transferred to researchers at Eglin AFB in Florida;
2. Training of Eglin AFB researchers: The project provided several onsite training and support events at Georgia Tech and Eglin AFB for researchers at Eglin AFB in Florida. The technical aspects of the training are: (a) application and execution of our CODEX software code suites, (b) generation of statistically similar microstructure sets for simulations, and (3) pre- and post-processing of data;
3. Technical support: support in terms of CODEX application, model preparation, and data analyses have been provided to researchers at the Eglin AFB; and
4. User manual, documentation, and material data have been provided to the Eglin AFB.

Journal Publications and Conference Proceedings

1. S. Kim, Y. Horie and M. Zhou, Ignition Desensitization of PBX via Aluminization, *Metallurgical & Materials Transactions A*, **46(10)**, 4578-4586, 2015;
2. D.B. Hardin, J.J. Rimoli and M. Zhou, Analysis of the Thermomechanical Response of Polycrystalline HMX under Impact Loading through High Fidelity Mesoscale Simulations, *AIP Advances* **4**, 097136, 2014;
3. S. Kim, A. Barua, Y. Horie and M. Zhou, Ignition Probability of PBXs Accounting for Multiple Sources of Material Stochasticity, *Journal of Applied Physics*, **115**, 174902, 2014;
4. A. Barua, S. Kim, Y. Horie and M. Zhou, Computational Analysis of Ignition in Heterogeneous Energetic Materials, *Materials Science Forum* **767**, 13-21, 2014;
5. A. Barua, S. Kim, Y. Horie and M. Zhou, Prediction of probabilistic ignition behavior of PBXs from microstructural stochasticity, *Journal of Applied Physics*, **113**, 184907, 2013;
6. A. Barua, S. Kim, Y. Horie and M. Zhou, Ignition Criterion for Heterogeneous Energetic Materials Based on Hotspot Size-Temperature Threshold, *Journal of Applied Physics*, **113**, 064906, 2013;
7. A. Barua and M. Zhou, Computational analysis of temperature rises in HMX-Estane PBXs, *Computational Mechanics*, **52**:151–159, 2013;
8. A. Barua, Y. Horie and M. Zhou, Microstructural level response of HMX-Estane PBX under effects of transient stress waves, *Proceedings of the Royal Society, Series A: Mathematical and Physical Sciences*, **468**, 3725-3744, 2012;

9. A. Barua, Y. Horie and M. Zhou, Energy localization in HMX-Estane PBXs during impact loading, *Journal of Applied Physics*, **111**, 054902, 2012;
10. A. Barua and M. Zhou, A Framework for Analyzing the Microstructure Level Thermomechanical Response of Polymer Bonded Explosives, *Materials Science Forum*, **673**, 21-33, (2011);
11. A. Barua and M. Zhou, A Lagrangian framework for analyzing microstructural level response of polymer bonded explosives, *Modeling and Simulation in Materials Science and Engineering*, **19** 055001, 1-24, 2011;
12. D. B. Hardin, Y. Horie, and M. Zhou, Ignition Sensitivity Behavior of an Novel HMX – Aluminum-bonded explosive (ABX), *Proceedings of the 19th APS Biennial Conference on Shock Compression of Condensed Matter (SCCM-2015)*, 2015;
13. B. Hardin and M. Zhou, Effect of Viscoplasticity on the Ignition Sensitivity of an HMX-Based PBX, *Proceedings of the 19th APS Biennial Conference on Shock Compression of Condensed Matter (SCCM-2015)*, 2015;
14. Y. Wu, F. Huang and M. Zhou, Microscopic modelling of ignition and burning for well-arranged energetic crystals in response to drop-weight impact, *Journal of Physics: Conference Series 500, 18th APS-SCCM and 24th AIRAPT*, 2014;
15. S. Kim, Y. Horie and M. Zhou. A Framework for Analyzing the Effect of Multiple Sources of Stochasticity on the Probabilistic Ignition of PBXs, *Proceedings of the 15th International Detonation Symposium (IDS)*, 2014; and
16. A. Barua and M. Zhou, Heating in Microstructures of HMX/ESTANE PBX During Dynamic Deformation, *Proceeding of The American Physical Society (APS) Shock Compression of Condensed Matter (SCCM) Conference*, 2011.

Presentations (♦ invited talk, invited keynote talk, invited plenary lecture, invited lecture, or invited seminar)

1. Ignition Sensitivity Behavior of an Novel HMX – Aluminum-bonded explosive (ABX), 19th APS Biennial Conference on Shock Compression of Condensed Matter (SCCM-2015), June 14-19, 2015, Tampa, FL;
2. Effect of Viscoplasticity on the Ignition Sensitivity of an HMX-Based PBX, 19th APS Biennial Conference on Shock Compression of Condensed Matter (SCCM-2015), June 14-19, 2015, Tampa, FL;
3. Ignition of pressed granular explosives due to short-duration pulse loading, 19th APS Biennial Conference on Shock Compression of Condensed Matter (SCCM-2015), June 14-19, 2015, Tampa, FL;
4. Computational Prediction of Hugh James Ignition Threshold of Pressed HMX, May 6, 2015, Eglin AFB, FL; ♦
5. Effect of load intensity on heating in a polymer-bonded explosive, 19th APS Biennial Conference on Shock Compression of Condensed Matter (SCCM-2015), June 14-19, 2015, Tampa, FL;

6. The Effect of Viscoplasticity in HMX Particles on the Mechanical Behavior and Ignition Sensitivity of PBXs, Mach Conference Symposium on Symposium on Energetic Materials: Coupling Modeling and Experiment, Mach Conference 2015, April 8-10, 2015, Annapolis, MD; ♦ with D. B. Hardin
7. Microstructural effects on initiation behavior in HMX, Mach Conference Symposium on Symposium on Energetic Materials: Coupling Modeling and Experiment, Mach Conference 2015, April 8-10, 2015, Annapolis, MD; ♦ with C. Molek, E. Welle, R. Wixom, K. Springer, H.S. Udaykumar, N. Rai, D. B. Hardin, S. Kim, C. Miller, M. Schmidt, and P. Samuels
8. Analysis of hotspot temperatures in a PBX under impact loading using a coupled chemical – thermomechanical framework, Annual AIChE Meeting, GA, Nov. 16-21, 2014;
9. Computational Prediction of Structure and Multiphysics Behavior of Materials, Sichuan University, Chengdu, China, November 14, 2014; ♦
10. Effect of Viscoplasticity in HMX Particles Grains on the Ignition Sensitivity probability of Dynamically Loaded PBXs, 51st Annual Technical Meeting of the Society of Engineering Science (SES), West Lafayette, Indiana, October 1-3, 2014;
11. Effect of aluminization on ignition sensitivity of PBX, 51st Annual Technical Meeting of the Society of Engineering Science (SES), West Lafayette, Indiana, October 1-3, 2014;
12. Effect of Multiple Sources of Material Stochasticity on the Probabilistic Ignition Behavior of PBXs, 15th International Detonation Symposium, (IDS), San Francisco, CA, July 13-18, 2014;
13. Quantifying the Effect of Rate-Dependent Plasticity of HMX Particles on the Mechanical Behavior and Ignition Sensitivity of PBXs, 15th International Detonation Symposium, (IDS), San Francisco, CA, July 13-18, 2014;
14. Energy efficiency of Li-alloy electrode during cyclic charge-discharge, 1st International Symposium on Energy Challenges and Mechanics, Aberdeen, Scotland, U.K., July 8-10, 2014; ♦
15. Computational Prediction of Structure and Multiphysics Behavior of Materials, National University of Ireland – Galway, Ireland, July 3, 2014; ♦
16. Computational Prediction of Structure and Multiphysics Behavior of Materials, University of Limerick, Limerick, Ireland, July 2, 2014; ♦
17. Probabilistic Ignition Behavior of PBXs from with Multiple Sources of Material Stochasticity, US National Congress on Theoretical and Applied Mechanics (USNCTAM), June 15-20, 2014, East Lansing, MI, USA;
18. Prediction of ignition probability of energetic materials from meso-scale tracking of hotspot dynamics, 2014 Gordon Research Conference on Energetic Materials – Forward Thinking: New Approaches, Concepts, and Paradigms Towards Understanding and Predicting EM Response, June 15-20, 2014, Sunday River Resort, Newry, ME; ♦
19. Novel Approach for Predicting the Ignition Behavior of Energetic Materials, May 15, 2014, Seoul National University, Seoul, Korea; ♦

20. Prediction of Ignition Behavior of Energetic Materials from Hotspot Dynamics, AFOSR Workshop on In-situ Dynamic Mesoscale Measurements of Reacting Energetic Materials, April 1, 2014, Arlington , VA; ♦
21. Prediction of Probabilistic Ignition Behavior of Heterogeneous Energetic Materials with Multiple Sources of Material Stochasticity, 2014 TMS Annual Meeting and Exhibition, February 16-20, 2014, San Diego Convention Center, San Diego, California; ♦
22. Latest developments in research on the ignition behavior of heterogeneous energetic materials, February 14, 2014, Eglin Air Force Base, Fort Walton Beach, FL; ♦
23. Computational prediction of ignition probability of PBXs, International Workshop on Intensive Loading and Its Effects, Beijing Institute of Technology, December 18, 2013, Beijing, China; ♦
24. Microstructure – probabilistic ignition behavior relations of heterogeneous energetic materials, Kumamoto University, November 13-15, 2013, Kumamoto, Japan; ♦
25. Computational Prediction of Probabilistic Ignition Behavior of PBXs from Microstructural Stochasticity, 50th SES Annual Technical Meeting and ASME-AMD Annual Summer Meeting, July 28-31, 2013, Providence, RI; ♦
26. Ignition Criterion for Heterogeneous Energetic Materials Based on Hotspot Size-Temperature Threshold, 50th SES Annual Technical Meeting and ASME-AMD Annual Summer Meeting, July 28-31, 2013, Providence, RI; ♦
27. Ignition Criterion for Energetic Materials based on critical size-temperature threshold of hotspot criticality. 12th U.S. National Congress on Computational Mechanics (USNCCM12), Raleigh, North Carolina, July 22-25, 2013;
28. Thermomechanical Response of HMX Polycrystals to Simulated Impact Loading, Intl. Conference of the APS Topical Group on Shock Compression of Condensed Matter (SCCM), July 7–12, 2013, Seattle, WA.
29. A framework for analyzing the ignition response of energetic materials under dynamic loading, SCCM, July 7–12, 2013, Seattle, WA.
30. Prediction of Probabilistic Ignition Behavior of PBXs from Microstructural Stochasticity, SCCM, July 7–12, 2013, Seattle, WA.
31. A Criterion for Predicting Probabilistic Ignition Behavior of Energetic Materials, the Laboratory of Nonlinear Mechanics, The Institute of Mechanics, Chinese Academy of Science, Beijing, China, April 17, 2013; ♦
32. An ignition criterion for heterogeneous energetic materials, International Symposium on Explosion, Shock wave and High-energy reaction Phenomena 2013 (ESHP 2013), March 27 - 29, 2013, Okinawa, Japan; ♦
33. Computational Prediction of the Stochastic Ignition Behavior of PBX, International Symposium on Explosion, Shock wave and High-energy reaction Phenomena 2013 (ESHP 2013), March 27 - 29, 2013, Okinawa, Japan; ♦

34. Ignition of Heterogeneous Energetic Materials, International Workshop on Intensive Loading and Its Effects, Beijing Institute of Technology, December 2, 2012, Beijing, China; ♦
35. Dynamic Response of Aluminized Polymer-Bonded Explosives, ASME International Mechanical Engineering Congress & Exposition (IMECE), Houston, Texas, November 9-15, 2012, with A. Barua;
36. Heating in Microstructures of HMX/Estane PBX during Dynamic Deformation, 49th SES Annual Technical Meeting, Georgia Tech, Atlanta, Georgia, October 10-12, 2012;
37. Crystalline plasticity as a source of hot spots in energetic molecular polycrystals, 49th SES Annual Technical Meeting, Georgia Tech, Atlanta, Georgia, October 10-12, 2012, with D. Barrett Hardin and J. Rimoli;
38. Crystalline plasticity as a source of hot spots in energetic molecular polycrystals, International Workshop on Computational Mechanics of Materials, Baltimore, MD, September 24-26, 2012, with D. B. Hardin and J. J. Rimoli;
39. Heating in Microstructures of HMX/Estane PBX during Dynamic Deformation, DTRA Basic Research Technical Review, July 23 – August 2, 2012, Springfield, VA;
40. A 3D Mesoscale Model for Impact Induced Heating in B-HMX, DTRA Basic Research Technical Review, July 23 – August 2, 2012, Springfield, VA;
41. Microstructural response of granular HMX to impact loading, DTRA Basic Research Technical Review, July 23 – August 2, 2012, Springfield, VA;
42. Multiscale/Multicomponent Modeling of Impact Response of Heterogeneous Energetic Materials, DTRA Basic Research Review, July 26, 2011, Springfield, VA;
43. Microstructural level response of HMX-Estane PBX under Effects of Transient Stress Waves, 10th World Congress on Computational Mechanics (WCCM 2012), São Paulo, Brazil, July 8-13, 2012, with A. Barua;
44. Micromechanical Simulations of the Dynamic Behavior of Polymer Bonded Explosives (PBX), Energetic Materials Gordon Conference, June 17-22, 2012, Mount Snow Resort, West Dover, VT;
45. A 3D Mesoscale Model for Impact Induced Heating in β -HMX, Energetic Materials Gordon Conference, June 17-22, 2012, Mount Snow Resort, West Dover, VT;
46. Numerical simulation of the microstructural level response of PBX to impulsive loading, December 6, 2011, AFRL Workshop on Dynamic Behavior of Energetic Materials, Eglin Air Force Base, Fort Walton Beach, FL; ♦
47. Computational modeling of the effects of material heterogeneity on dynamic response at different scales, Air Force Workshop on High-rate Deformation Physics of Heterogeneous Materials, July 28, 2011, Arlington, VA; ♦
48. Micromechanical Simulations of the Dynamic Behavior of Polymer Bonded Explosives (PBX), DTRA Basic Research Review, July 28, 2011, Springfield, VA;
49. A 3D Microstructural Level Model for Analyzing the Response of Polymer Bonded Explosives, DTRA Basic Research Review, July 28, 2011, Springfield, VA;

50. Multiscale/Multicomponent Modeling of Impact Response of Heterogeneous Energetic Materials, DTRA Basic Research Review, July 28, 2011, Springfield, VA;
51. A Lagrangian Framework for Analyzing the Deformation, Fracture and Heating of PBXs, The American Physical Society (APS) Shock Compression of Condensed Matter (SCCM) Conference, Chicago, IL, June 26 - July 1, 2011; ♦
52. A 3-D microstructural level model for analyzing the response of polymer bonded explosives, The American Physical Society (APS) Shock Compression of Condensed Matter (SCCM) Conference, Chicago, IL, June 26 - July 1, 2011;
53. Heating in Microstructures of HMX/Estane PBX during Dynamic Deformation, The American Physical Society (APS) Shock Compression of Condensed Matter (SCCM) Conference, Chicago, IL, June 26 - July 1, 2011, with A. Barua;
54. Mesoscale CFEM simulations of the impact response of energetic composites, AFOSR/LLNL/AFRL/ARO Workshop on Particulate Materials in Extreme Environments (PMEE 2010), September 20-24, 2010, Lawrence Livermore National Laboratory, Livermore, CA; ♦
55. Mesoscale CFEM simulation of failure and hot-spot formation in PBX under impact loading, ISWI 2010 Conference, The Shock and High Rate Properties of Matter, September 7-10, 2010, University of Cambridge, U.K.; ♦
56. Microstructural Level Response of Polymer Bonded Explosives under Impact Loading, The 3rd International Symposium on Explosion, Shock Wave and High-energy Reaction Phenomena 2010 (3rd ESHP Symposium), September 1-3, 2010, Seoul National University, Seoul Korea; ♦
57. CFEM Simulation of the Response of Polymer Bonded Explosives, Research and Engineering Education Facility, University of Florida, Shalimar, Florida, July 14-16, 2010; ♦ and
58. Micromechanical Simulations of Impact Loading on Polymer Bonded Explosives, 16th US National Congress of Theoretical and Applied Mechanics, June 27 - July 2, 2010, State College, PA.

What do you plan to do during the next reporting period to accomplish the goals?

If there are no changes to the agency-approved application or plan for this effort, state "No Change."

Describe briefly what you plan to do during the next reporting period to accomplish the goals and objectives.

We have accomplished the project goals.

DISTRIBUTION LIST
DTRA-TR-16-67

DEPARTMENT OF DEFENSE

DEFENSE THREAT REDUCTION
AGENCY
8725 JOHN J. KINGMAN ROAD
STOP 6201
FORT BELVOIR, VA 22060
ATTN: A. DALTON

DEFENSE TECHNICAL
INFORMATION CENTER
8725 JOHN J. KINGMAN ROAD,
SUITE 0944
FT. BELVOIR, VA 22060-6201
ATTN: DTIC/OCA

**DEPARTMENT OF DEFENSE
CONTRACTORS**

QUANTERION SOLUTIONS, INC.
1680 TEXAS STREET, SE
KIRTLAND AFB, NM 87117-5669
ATTN: DTRIAC